Supplementary Information for

"Theoretical investigation on the interaction between Rh$^{\text{III}}$ octaethylporphyrin and a graphite basal surface: A comparison study of DFT, DFT-D, and AFM"

Kohei Tada[a*], Yasushi Maeda[a], Hiroyuki Ozaki[a], Shingo Tanaka[a], Shin-ichi Yamazaki[a]

[a] *Research Institute of Electrochemical Energy, National Institute of Advanced Industrial Science and Technology (AIST), 1-8-31, Midorigaoka, Ikeda, Osaka 563-8577, Japan*

[*]Corresponding author
Phone: +81-72-751-8566
Fax: +81-72-751-9714
E-mail address: k-tada@aist.go.jp

Contents

Results of benchmark calculations for Rh atom, Rh cations (Rh$^+$, Rh^{2+}, and Rh^{3+}), and Rh anion (Rh$^-$)

Computational costs of high-accuracy first principles methods, such as post-HF and multi-reference methods [S1], are high; therefore, they can be only adopted for calculations of systems characterized by small numbers of atoms, and we cannot use these methods to perform calculations on metalloporphyrins. On the other hand, computational costs of DFT-based calculations [S2] are comparatively lower than the high-accuracy methods. However, results of DFT-based calculations often dependent on the selection of the exchange-correlation functional and basis set, and the results sometimes do not, even qualitatively, agree with the experimental data. Hence, the dependencies of the exchange-correlation functional and basis set should be investigated in detail.

We performed benchmark calculations for the ionization energies (first, second, and third) and electron affinity of the Rh atom. Nine exchange-correlation functionals were considered, namely, BLYP [S3], PBEPBE [S4], B3LYP [S5], B3PW91 [S6], PBE0 [S7], M05 [S8], M06 [S9], CAM-B3LYP [S10], and LC-ωPBE [S11]. Five basis sets were considered for the Rh atom, namely, SDD [S12], LANL2DZ [S13], LANL08(f) [S14], LANL2DZ+1d1f [S15], LANL-[10s8p7d3f2g] [S15]. Serial numbers for the combination of exchange-correlation functionals and basis sets are summarized in Table S1. For reference to high-accuracy calculations, coupled-cluster singlet and doublet with a triplet contribution (CCSD(T)) [S16] calculations with the LANL-[10s8p7d3f2g] basis set were carried out. The calculation results were compared with experimental results [S17]. The calculations were performed using the Gaussian 09 program package [S18].

The calculation results are summarized in Fig. S1 and Tables S2–S4. Fig. S1 shows all calculation results. Tables S2 and S3 show the results obtained for the first ionization energy and electron affinity by DFT calculations characterized by values close to the experimental results, respectively. Table S4 shows the summation of the second and third ionization energy by DFT calculations characterized by values close to the experimental results.

As observed, the effect of the selection of different exchange-correlation functionals and basis sets on the first, second, third ionization energies and electron affinity of Rh is very small.

When investigating the electro-oxidation of CO by Rh porphyrin complexes, the redox potential of Rh^{III} ⇌ Rh^I is a crucial factor to consider, since CO oxidation is a two-electron oxidation. Here, the redox potential corresponds to the summation of the second and third ionization energies, which are summarized in Table S4. The results in Table S4 showed that PBE-based functionals are a better choice than other functionals for estimating the redox potential.

Table S1. Serial numbers of the combination of exchange-correlation functionals and basis sets for the benchmark calculation of ionization energy and electron affinity of Rh atom.

| Serial number	Exchange-correlation functional	Basis set	Serial number	Exchange-correlation functional	Basis set
1	BLYP	SDD	26	M05	SDD
2	BLYP	LANL2DZ	27	M05	LANL2DZ
3	BLYP	LANL08(f)	28	M05	LANL08(f)
4	BLYP	LANL2DZ+1d1f	29	M05	LANL2DZ+1d1f
5	BLYP	LANL-[10s8p7d3f2g]	30	M05	LANL-[10s8p7d3f2g]
6	PBEPBE	SDD	31	M06	SDD
7	PBEPBE	LANL2DZ	32	M06	LANL2DZ
8	PBEPBE	LANL08(f)	33	M06	LANL08(f)
9	PBEPBE	LANL2DZ+1d1f	34	M06	LANL2DZ+1d1f
10	PBEPBE	LANL-[10s8p7d3f2g]	35	M06	LANL-[10s8p7d3f2g]
11	B3LYP	SDD	36	CAM-B3LYP	SDD
12	B3LYP	LANL2DZ	37	CAM-B3LYP	LANL2DZ
13	B3LYP	LANL08(f)	38	CAM-B3LYP	LANL08(f)
14	B3LYP	LANL2DZ+1d1f	39	CAM-B3LYP	LANL2DZ+1d1f
15	B3LYP	LANL-[10s8p7d3f2g]	40	CAM-B3LYP	LANL-[10s8p7d3f2g]
16	B3PW91	SDD	41	LC-ωPBE	SDD
17	B3PW91	LANL2DZ	42	LC-ωPBE	LANL2DZ
18	B3PW91	LANL08(f)	43	LC-ωPBE	LANL08(f)
19	B3PW91	LANL2DZ+1d1f	44	LC-ωPBE	LANL2DZ+1d1f
20	B3PW91	LANL-[10s8p7d3f2g]	45	LC-ωPBE	LANL-[10s8p7d3f2g]
21	PBE0	SDD			
22	PBE0	LANL2DZ			
23	PBE0	LANL08(f)			
24	PBE0	LANL2DZ+1d1f			
25	PBE0	LANL-[10s8p7d3f2g]			
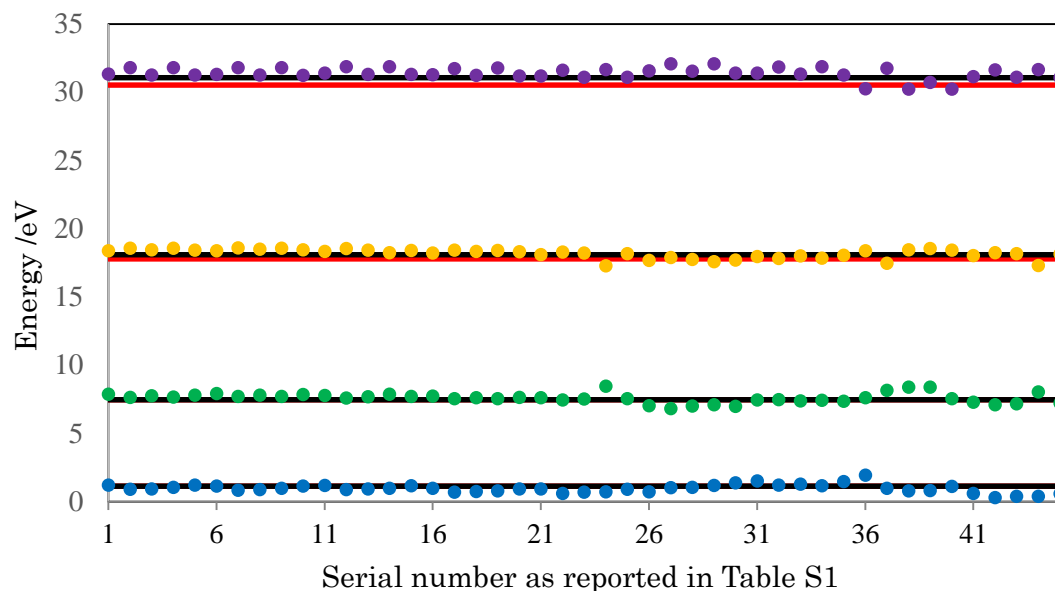
Fig. S1. First (green dots), second (yellow dots), and third (purple dots) ionization energies and electron affinity (blue dots) of Rh atom as estimated by DFT calculations. Black lines represent the values of experimental data and red lines indicate the values obtained by CCSD(T) calculations.

Table S2. First ionization energies estimated by DFT calculations characterized by values close to experimental data.

Ranking	Exchange-correlation functional	Basis set	Estimated value /eV	Deviation from the experimental value
1	M06	LANL2DZ	7.47	0 %
2	M06	SDD	7.46	0 %
3	PBE0	LANL2DZ	7.44	0 %
4	PBE0	LANL08(f)	7.51	1 %
4	M06	LANL2DZ+1d1f	7.43	1 %
6	B3PW91	LANL2DZ	7.54	1 %
6	B3PW91	LANL2DZ+1d1f	7.54	1 %
6	PBE0	LANL-[10s8p7d3f2g]	7.54	1 %
	Experimental value		7.47	0 %
	Estimation value by CCSD(T)		7.47	0 %

Table S3. First electron affinities estimated by DFT calculations characterized by values close to experimental data.

Ranking	Exchange-correlation functional	Basis set	Estimated value /eV	Deviation from the experimental value
1	PBEPBE	LANL-[10s8p7d3f2g]	1.13	0 %
2	PBEPBE	SDD	1.15	2 %
2	CAM-B3LYP	LANL-[10s8p7d3f2g]	1.11	2 %
4	B3LYP	LANL-[10s8p7d3f2g]	1.16	3 %
5	M06	LANL2DZ+1d1f	1.17	4 %
	Experimental value		1.13	0 %
	Estimation value by CCSD(T)		1.12	1 %

Table S4. Summation of the second (IE2) and third (IE3) ionization energies estimated by DFT calculations characterized by values close to experimental data.

Ranking	Exchange-correlation functional	Basis set	IE2 /eV	IE3 /eV	Sum /eV	Deviation from the experimental value
1	LC-ωPBE	LANL-[10s8p7d3f2g]	18.14	31.08	49.22	0 %
2	PBE0	SDD	18.10	31.18	49.28	0 %
3	PBE0	LANL08(f)	18.17	31.09	49.26	1 %
4	LC-ωPBE	SDD	18.04	31.15	49.19	1 %
5	PBE0	LANL-[10s8p7d3f2g]	18.18	31.10	49.28	1 %
6	PBE0	LANL08(f)	18.22	31.09	49.31	1 %
7	M06	LANL-[10s8p7d3f2g]	18.05	31.25	49.30	1 %
8	M06	LANL08(f)	18.01	31.34	49.35	1 %
	Experimental value		18.08	31.06	49.14	0 %
	Estimation value by CCSD(T)		17.78	30.52	48.30	3 %

Results of benchmark calculations for [RhCO]^x (x = +1, 0, and –1) molecules

Benchmark calculations for CO-coordinated Rh molecules ([RhCO]$^+$, [Rh(CO)], and [RhCO]$^–$) were performed to investigate the exchange-correlation functional and basis set dependencies. The basis sets considered for C and O atoms were 6-31G(d) [S19], cc-pVDZ [S20], 6-31+G(d) [S19], aug-cc-pVDZ [S20], 6-311G(d) [S19], cc-pVTZ [S20], 6-311+G(d) [S19], aug-cc-pVTZ [S20], cc-pVQZ [S20], aug-cc-pVQZ [S20], cc-pV5Z [S20], aug-cc-pV5Z [S20], cc-pV6Z [S20], and aug-cc-pV6Z [S20]. Exchange-correlation functionals and basis sets for Rh that show comparatively better results for Rh ionization energies and electron affinity were considered. Serial numbers for combinations of exchange-correlation functionals and basis sets are reported in Table S5. The Gaussian 09 program package was used for the benchmark calculations.

We analyzed the benchmark results for the distance between Rh and C (Fig. S2), distance between C and O (Fig. S3), the vibrational frequency of the Rh–C bond (Fig. S4), vibrational frequency of the C–O bond (Fig. S5), the energy difference among the total energies of [RhCO]^x molecules (Fig. S6), and the CO adsorption energy (Fig. S7), estimated as $E([RhCO]^x) – E(Rh^x) – E(CO)$. All the structures of the molecules were optimized by all the considered methods, and vibration frequency analysis was performed for all the optimized structures.

Figure S2 shows that there is no qualitative dependence of the distance between Rh and C in [RhCO]^x molecules on the DFT computational method, except for the results of serial numbers 7 and 17, which are the results obtained by the M06 functional. The reason why the results of serial number 7 and 17 are different from that obtained with other functionals can be understood observing the results of the vibrational frequency of the Rh–C bond shown in Fig. S4. The vibrational frequencies of [RhCO]$^+$ estimated using the methods of serial numbers 7 and 17 are imaginary, so the results could not be shown in Fig. S4. In other words, the methods optimized the geometry of [RhCO]$^+$ to transition states (they will be artificial states) of CO adsorption onto Rh$^+$. This occurred because we did not calculate the frequencies of all sequential structures during geometry optimization, in order to lower the computational cost. Except for the results of serial number 7 and 17, the results shown in Fig. S4 (the vibrational frequency of Rh–C bond) are qualitatively the same.

As reported in Fig. S3, there is no dependency of the C-O bond distance on the calculation methods. Hence, there is little dependence of the method on the vibrational frequency of the C–O bond (Fig. S5), and the results agree with the experimental data [S15].

The estimated energy differences among the total energies of [RhCO]^x molecules are qualitatively not affected by the computational method (Fig. S6). Additionally, as the results in Fig. S7 show, the orders of magnitude of the CO adsorption energies of Rh^x species as estimated by DFT calculations are the same, and the order of magnitude is identical to that obtained by CCSD(T) with LANL- [10s8p7d3f2g] (for Rh) and aug-cc-pVQZ (for C and O) basis sets. However, as the results obtained by M06 functional show, e.g. serial numbers 5–8, the differences between CO adsorption energy onto Rh and Rh$^–$ respectively are very small, and differences in the results with respect to other functionals or CCSD(T) calculations can be observed. Hence, the M06 functional may be unsuitable for calculation on molecular complexes including the Rh–CO coordination bond.

In summary, the benchmark calculations demonstrate that the dependence of the calculation results of

Rh-CO molecular complexes on the DFT calculation method employed is relatively small; especially, the basis set dependency is very small.

Table S5. Serial numbers of the combinations of exchange-correlation functionals and basis sets for the benchmark calculation of [RhCO]^x (x = +1, 0, and −1) molecules.

Serial number	Exchange-correlation functional	Basis set for Rh	Basis set for C	Basis set for O
1	PBE0	SDD	6-31+G*	6-31+G*
2	PBE0	SDD	6-31G*	6-31+G*
3	PBE0	SDD	aug-cc-pVDZ	aug-cc-pVDZ
4	PBE0	SDD	cc-pVDZ	aug-cc-pVDZ
5	M06	SDD	6-31+G*	6-31+G*
6	M06	SDD	6-31G*	6-31+G*
7	M06	SDD	aug-cc-pVDZ	aug-cc-pVDZ
8	M06	SDD	cc-pVDZ	aug-cc-pVDZ
9	PBE0	LANL2DZ	6-31+G*	6-31+G*
10	PBE0	LANL2DZ	6-31G*	6-31+G*
11	PBE0	LANL2DZ	aug-cc-pVDZ	aug-cc-pVDZ
12	PBE0	LANL2DZ	cc-pVDZ	aug-cc-pVDZ
13	M06	LANL2DZ	6-31+G*	6-31+G*
14	M06	LANL2DZ	6-31G*	6-31+G*
15	M06	LANL2DZ	aug-cc-pVDZ	aug-cc-pVDZ
16	M06	LANL2DZ	cc-pVDZ	aug-cc-pVDZ
17	PBEPBE	LANL-[10s8p7d3f2g]	aug-cc-pVQZ	aug-cc-pVQZ
18	PBEPBE	LANL-[10s8p7d3f2g]	cc-pVQZ	aug-cc-pVQZ
19	PBEPBE	LANL-[10s8p7d3f2g]	aug-cc-pV5Z	aug-cc-pV5Z
20	PBEPBE	LANL-[10s8p7d3f2g]	cc-pV5Z	aug-cc-pV5Z
21	PBEPBE	LANL-[10s8p7d3f2g]	aug-cc-pV6Z	aug-cc-pV6Z
22	PBEPBE	LANL-[10s8p7d3f2g]	cc-pV6Z	aug-cc-pV6Z
23	CAM-B3LYP	LANL-[10s8p7d3f2g]	aug-cc-pVQZ	aug-cc-pVQZ
24	CAM-B3LYP	LANL-[10s8p7d3f2g]	cc-pVQZ	aug-cc-pVQZ
25	CAM-B3LYP	LANL-[10s8p7d3f2g]	aug-cc-pV5Z	aug-cc-pV5Z
26	CAM-B3LYP	LANL-[10s8p7d3f2g]	cc-pV5Z	aug-cc-pV5Z
27	CAM-B3LYP	LANL-[10s8p7d3f2g]	aug-cc-pV6Z	aug-cc-pV6Z
28	CAM-B3LYP	LANL-[10s8p7d3f2g]	cc-pV6Z	aug-cc-pV6Z
29	LC-ωPBE	LANL-[10s8p7d3f2g]	aug-cc-pVQZ	aug-cc-pVQZ
30	LC-ωPBE	LANL-[10s8p7d3f2g]	cc-pVQZ	aug-cc-pVQZ
31	LC-ωPBE	LANL-[10s8p7d3f2g]	aug-cc-pV5Z	aug-cc-pV5Z
32	LC-ωPBE	LANL-[10s8p7d3f2g]	cc-pV5Z	aug-cc-pV5Z
33	LC-ωPBE	LANL-[10s8p7d3f2g]	aug-cc-pV6Z	aug-cc-pV6Z

34	LC-ωPBE	LANL-[10s8p7d3f2g]	cc-pV6Z	aug-cc-pV6Z
35	PBEPBE	SDD	6-31+G*	6-31+G*
36	PBEPBE	SDD	6-31G*	6-31+G*
37	PBEPBE	SDD	aug-cc-pVDZ	aug-cc-pVDZ
38	PBEPBE	SDD	cc-pVDZ	aug-cc-pVDZ
39	B3PW91	LANL2DZ	6-31+G*	6-31+G*
40	B3PW91	LANL2DZ	6-31G*	6-31+G*
41	B3PW91	LANL2DZ	aug-cc-pVDZ	aug-cc-pVDZ
42	B3PW91	LANL2DZ	cc-pVDZ	aug-cc-pVDZ
43	B3PW91	LANL2DZ+1d1f	6-311+G*	6-311+G*
44	B3PW91	LANL2DZ+1d1f	6-311G*	6-311+G*
45	B3PW91	LANL2DZ+1d1f	aug-cc-pVTZ	aug-cc-pVTZ
46	B3PW91	LANL2DZ+1d1f	cc-pVTZ	aug-cc-pVTZ
47	M06	LANL2DZ+1d1f	6-311+G*	6-311+G*
48	M06	LANL2DZ+1d1f	6-311G*	6-311+G*
49	M06	LANL2DZ+1d1f	aug-cc-pVTZ	aug-cc-pVTZ
50	M06	LANL2DZ+1d1f	cc-pVTZ	aug-cc-pVTZ
51	PBE0	LANL08(f)	6-311+G*	6-311+G*
52	PBE0	LANL08(f)	6-311G*	6-311+G*
53	PBE0	LANL08(f)	aug-cc-pVTZ	aug-cc-pVTZ
54	PBE0	LANL08(f)	cc-pVTZ	aug-cc-pVTZ
55	M06	LANL08(f)	6-311+G*	6-311+G*
56	M06	LANL08(f)	6-311G*	6-311+G*
57	M06	LANL08(f)	aug-cc-pVTZ	aug-cc-pVTZ
58	M06	LANL08(f)	cc-pVTZ	aug-cc-pVTZ
59	LC-ωPBE	LANL08(f)	6-311+G*	6-311+G*
60	LC-ωPBE	LANL08(f)	6-311G*	6-311+G*
61	LC-ωPBE	LANL08(f)	aug-cc-pVTZ	aug-cc-pVTZ
62	LC-ωPBE	LANL08(f)	cc-pVTZ	aug-cc-pVTZ
63	B3LYP	LANL-[10s8p7d3f2g]	aug-cc-pVQZ	aug-cc-pVQZ
64	B3LYP	LANL-[10s8p7d3f2g]	cc-pVQZ	aug-cc-pVQZ
65	B3LYP	LANL-[10s8p7d3f2g]	aug-cc-pV5Z	aug-cc-pV5Z
66	B3LYP	LANL-[10s8p7d3f2g]	cc-pV5Z	aug-cc-pV5Z
67	B3LYP	LANL-[10s8p7d3f2g]	aug-cc-pV6Z	aug-cc-pV6Z
68	B3LYP	LANL-[10s8p7d3f2g]	cc-pV6Z	aug-cc-pV6Z
69	PBE0	LANL-[10s8p7d3f2g]	aug-cc-pVQZ	aug-cc-pVQZ
70	PBE0	LANL-[10s8p7d3f2g]	cc-pVQZ	aug-cc-pVQZ
71	PBE0	LANL-[10s8p7d3f2g]	aug-cc-pV5Z	aug-cc-pV5Z
72	PBE0	LANL-[10s8p7d3f2g]	cc-pV5Z	aug-cc-pV5Z

73	PBE0	LANL-[10s8p7d3f2g]	aug-cc-pV6Z	aug-cc-pV6Z
74	PBE0	LANL-[10s8p7d3f2g]	cc-pV6Z	aug-cc-pV6Z
75	M06	LANL-[10s8p7d3f2g]	aug-cc-pVQZ	aug-cc-pVQZ
76	M06	LANL-[10s8p7d3f2g]	cc-pVQZ	aug-cc-pVQZ
77	M06	LANL-[10s8p7d3f2g]	aug-cc-pV5Z	aug-cc-pV5Z
78	M06	LANL-[10s8p7d3f2g]	cc-pV5Z	aug-cc-pV5Z
79	M06	LANL-[10s8p7d3f2g]	aug-cc-pV6Z	aug-cc-pV6Z
80	M06	LANL-[10s8p7d3f2g]	cc-pV6Z	aug-cc-pV6Z
81	LC-ωPBE	SDD	6-31+G*	6-31+G*
82	LC-ωPBE	SDD	6-31G*	6-31+G*
83	LC-ωPBE	SDD	aug-cc-pVDZ	aug-cc-pVDZ
84	LC-ωPBE	SDD	cc-pVDZ	aug-cc-pVDZ
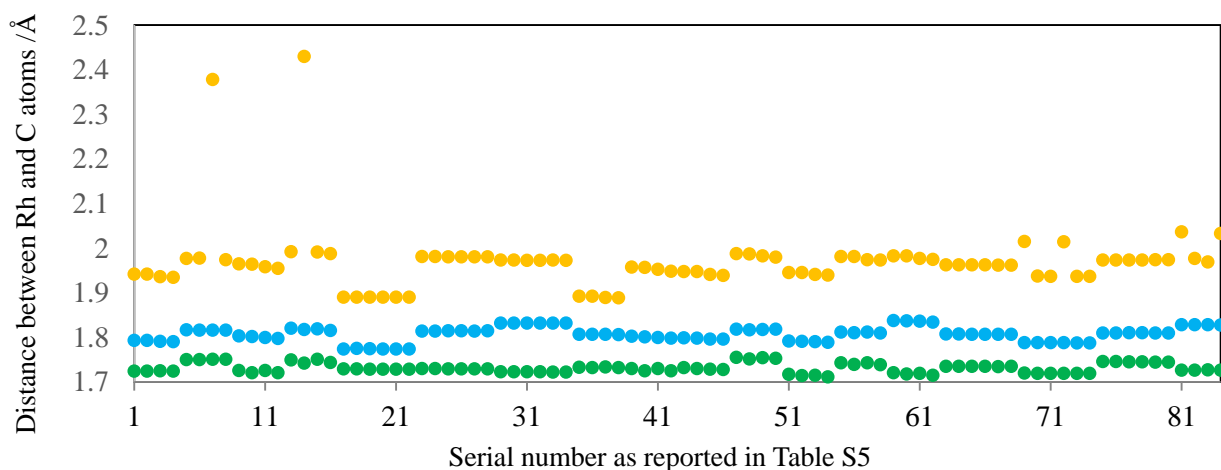
Fig. S2. Distance between Rh and C atoms in [RhCO]⁺ (yellow dots), [RhCO] (blue dots), and [RhCO]⁻ (green dots) molecules as obtained from DFT calculations.
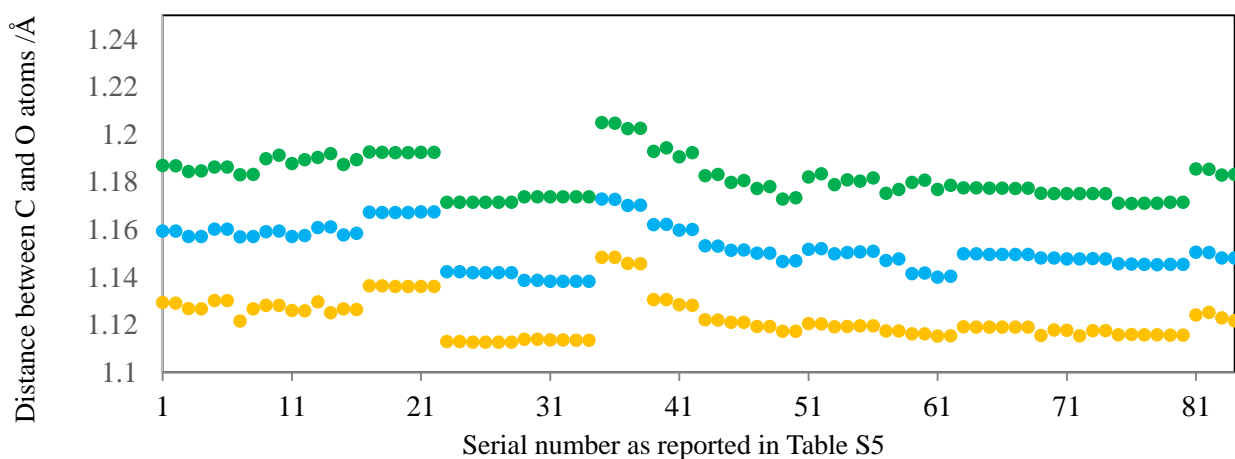
Fig. S3. Distance between C and O atoms in [RhCO]⁺ (yellow dots), [RhCO] (blue dots), and [RhCO]⁻ (green dots) molecules as obtained from DFT calculations.
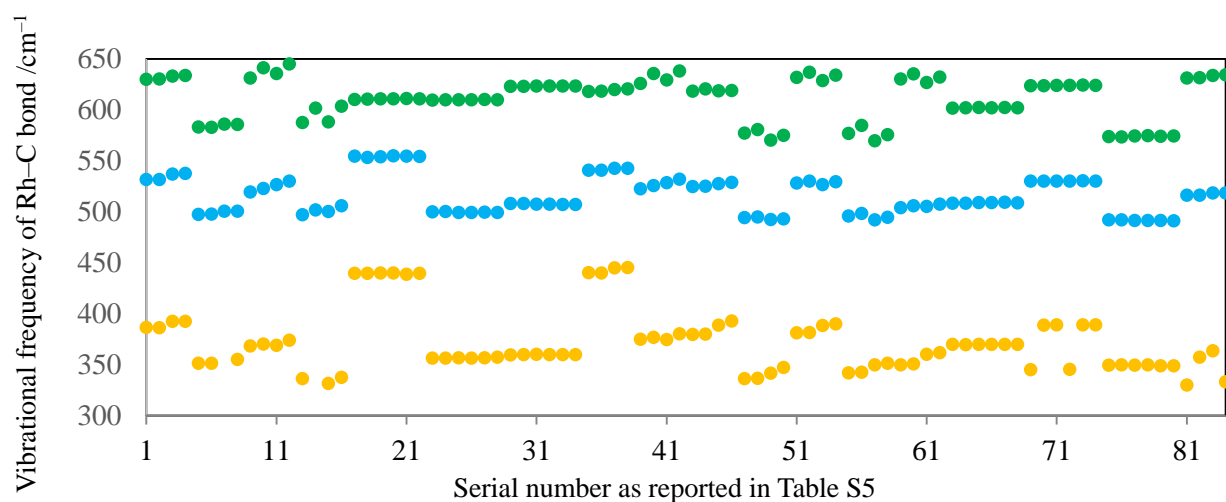
Fig. S4. Vibrational frequency of the Rh–C bond in [RhCO]$^+$ (yellow dots), [RhCO] (blue dots), and [RhCO]$^-$ (green dots) molecules as estimated by DFT calculations.
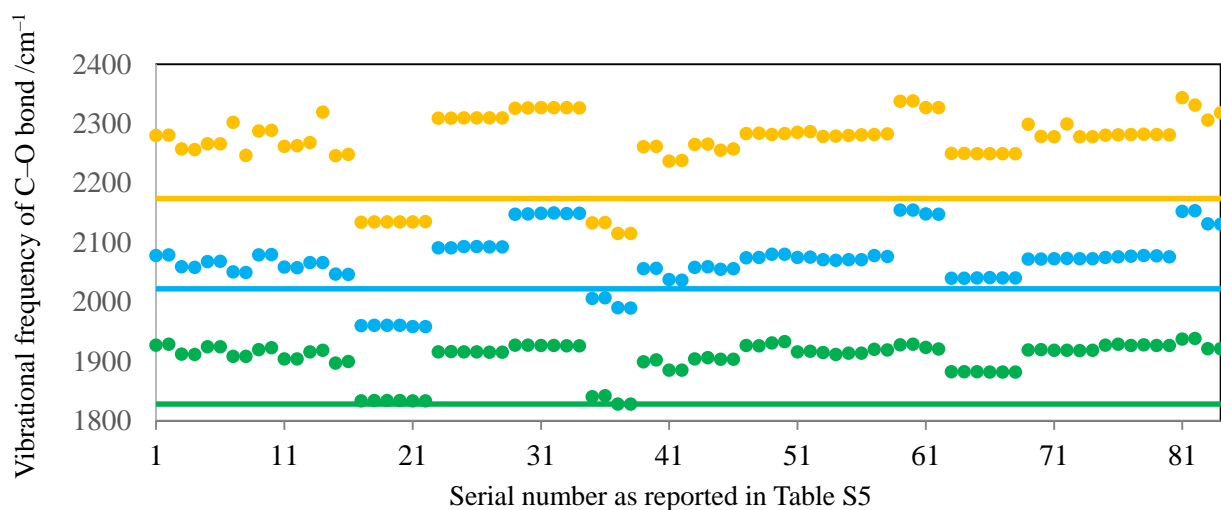
Fig. S5. Vibrational frequency of the C–O bond in [RhCO]$^+$ (yellow dots), [RhCO] (blue dots), and [RhCO]$^-$ (green dots) molecules as estimated by DFT calculations. The yellow, blue, and green lines represent the experimental results for [RhCO]$^+$, [RhCO], and [RhCO]$^-$, respectively.
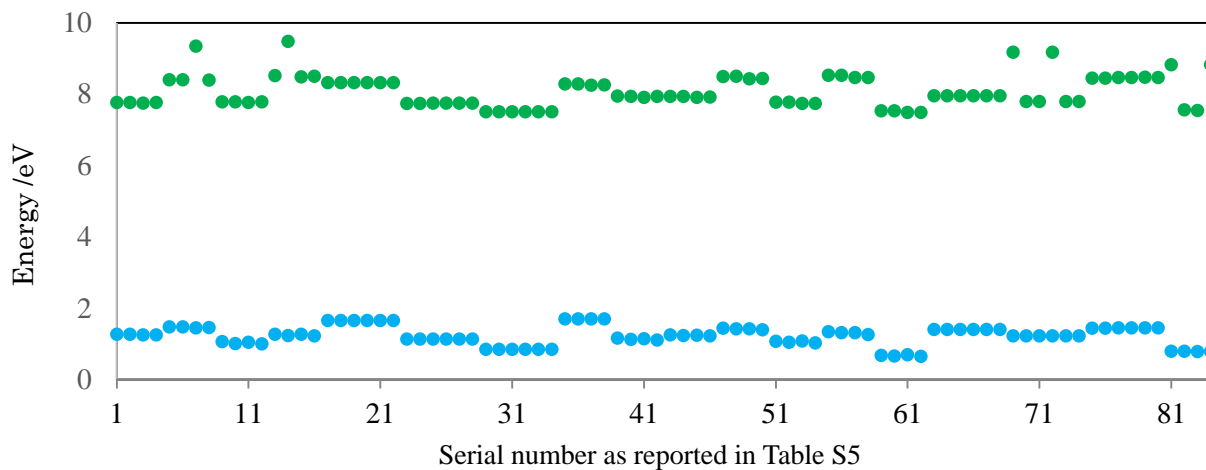
Fig. S6. Ionization energies (green dots) and electron affinities (blue dots) of the [RhCO] molecule as estimated by DFT calculations.
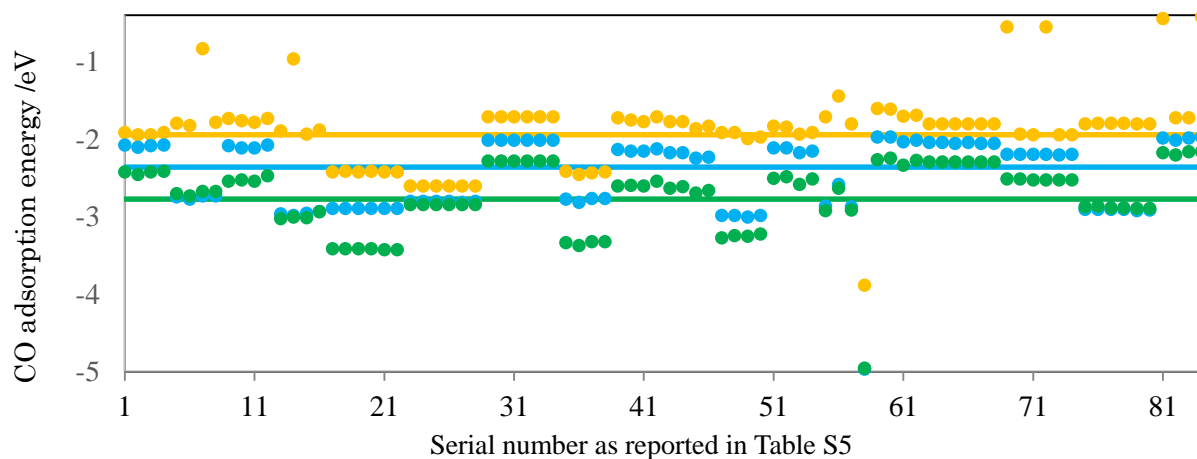
Fig. S7. CO adsorption energies of Rh^+ (yellow dots), Rh (blue dots), and Rh^- (green dots) as estimated by DFT calculations. The yellow, blue, and green lines represent the CCSD(T) calculation results for Rh^+, Rh, and Rh^-, respectively.

Adsorption energy of CO adsorption onto [Rh^{III}(OEP)(Cl)] complex with and without correction of BSSE

When different basis sets are used for different atoms, basis set superposition error (BSSE) occurs. BSSE is the error incurred when stabilization caused by the interaction between two (or more) molecules (atoms) is overestimated because one molecule uses the basis function of the other molecules to provide basis set flexibility of the molecule. Hence, the adsorption energy is generally overestimated when BSSE is not corrected. The effects of BSSE on the adsorption energy are usually discussed using a counterpoise scheme, which is a correction scheme for BSSE [S21].

We estimated the adsorption energies of CO adsorption onto [Rh^{III}(OEP)(Cl)] with and without a correction of BSSE using a counterpoise (CP) scheme. Owing to computational cost, it is hard to carry out geometry optimization with the CP method; therefore, the CO adsorption energies were estimated using the structure obtained by the calculations without the BSSE correction. For the CP scheme, [Rh^{III}(OEP)(CO)(Cl)] was separated into three fragments: [Rh^{III}(OEP)]$^+$, CO, and Cl$^-$. Similarly, the [Rh^{III}(OEP)(Cl)] was separated into two fragments: [Rh^{III}(OEP)]$^+$ and Cl$^-$.

The estimated adsorption energies with and without the correction were –1.17 eV and –1.29 eV, respectively. It was confirmed that a BSSE of 0.12 eV was included in CO adsorption energy. However, we did not discuss the CO adsorption energy in the main text, and the results and discussion were not affected.

Comparison of the results obtained by atom-centered and plane-wave basis sets

In the main text, we used two different computational approaches, an atom-centered basis set (Section 3.1) and plane-wave basis set (Section 3.2), using two major software packages (Gaussian09 [S18] and VASP [S22]). This is not a common practice. Therefore, we should perform a comparison of the results for the [Rh^{III}(OEP)(Cl)] complex using the two approaches (programs).

Figures S8 shows the geometries of the [Rh^{III}(OEP)(Cl)] complex optimized using a hybrid-DFT exchange-correlational functional, PBE0 [S7], with an atom-centered basis using the Gaussian09 program package. Basis sets for Rh, C and others were SDD [S12], 6-31G(d) [S19], and 6-31+G(d,p) [S19], respectively.

Figures S9-S11 show the optimized geometries for the [Rh^{III}(OEP)(Cl)] complex found using the VASP program package. The basis set was a projector-augmented-wave (PAW) [S23]. The results shown in Figs. S9, S10, and S11 were obtained by pure-DFT [S2], DFT-D2 [S24], and DFT-D3 [S25] methods, respectively. The exchange-correlational functional is PBE.

As shown in Figs. S8-S11, it is confirmed that the geometry of the [Rh^{III}(OEP)(Cl)] complex was not affected by the atom-centered (Fig. S8) and plane-wave (Figs. S9-S11) basis sets. In addition, the results were not affected by the DFT method: hybrid-DFT (Fig. S8), pure-DFT (Fig. S9), DFT-D2 (Fig. S10), and DFT-D3 (Fig.S11).

In the main text, we argued that the LUMO of [Rh^{III}(OEP)(Cl)] will be important for the interactions of [Rh^{III}(OEP)(Cl)] and graphite during CO electro-oxidation. Then, we checked the LUMOs by hybrid-DFT/SDD (for Rh), 6-31G(d) (for C), and 6-31+G(d,p) (for others) and DFT-D2/PAW methods. The VESTA [S26] and Advance/PHASE programs were used for visualization of calculated results. Figure S12 shows the results, and it was found that the LUMOs are similar one-electron wavefunctions.

Side view

: Rh atom
: Cl atom
: C atom
: N atom
: H atom

Top view
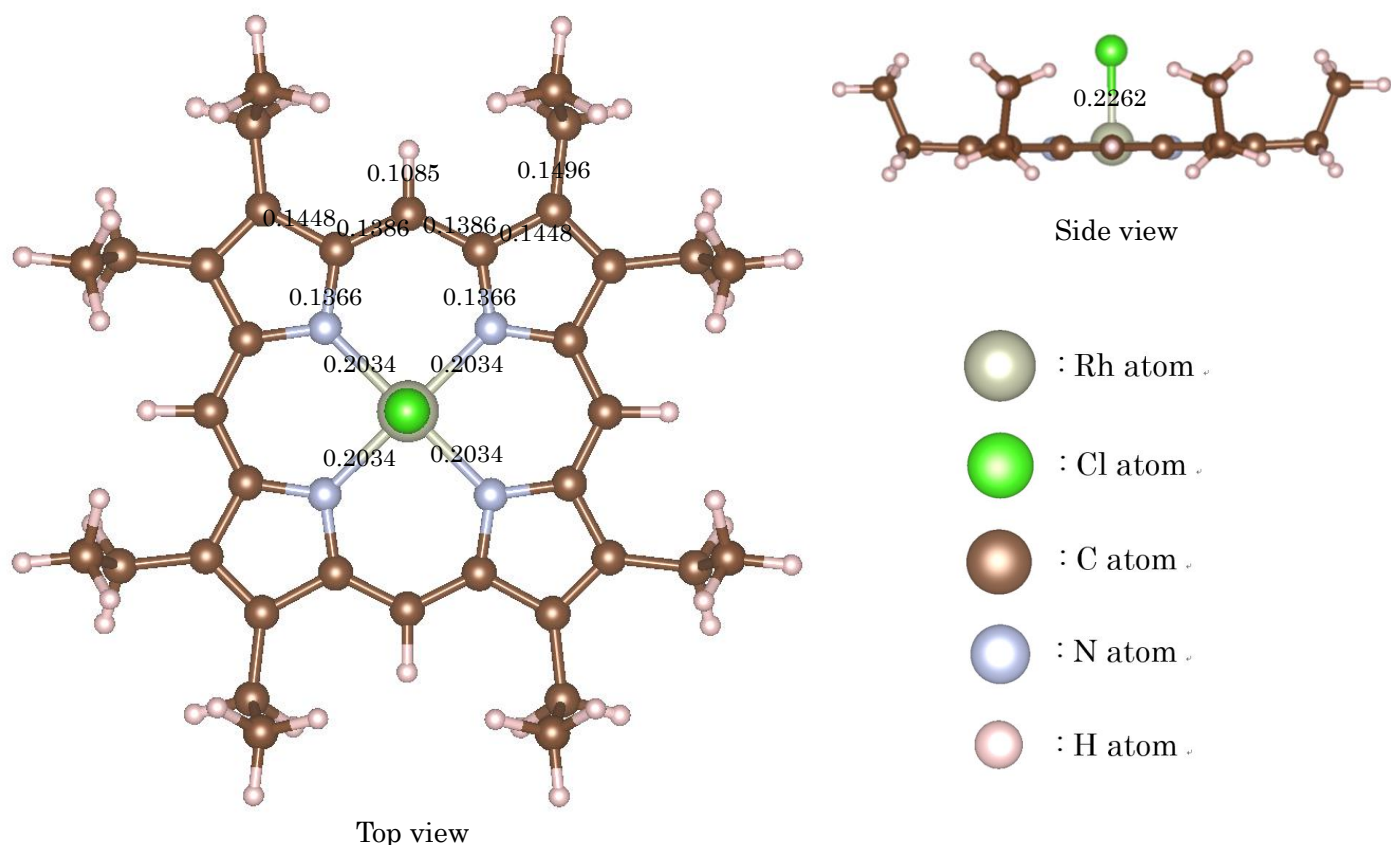
Fig. S8 The optimized geometry of [Rh^{III}(OEP)(Cl)] by PBE0/SDD (for Rh), 6-31G(d) (for C), and 6-31+G(d,p) (for others). The unit of length is nm.
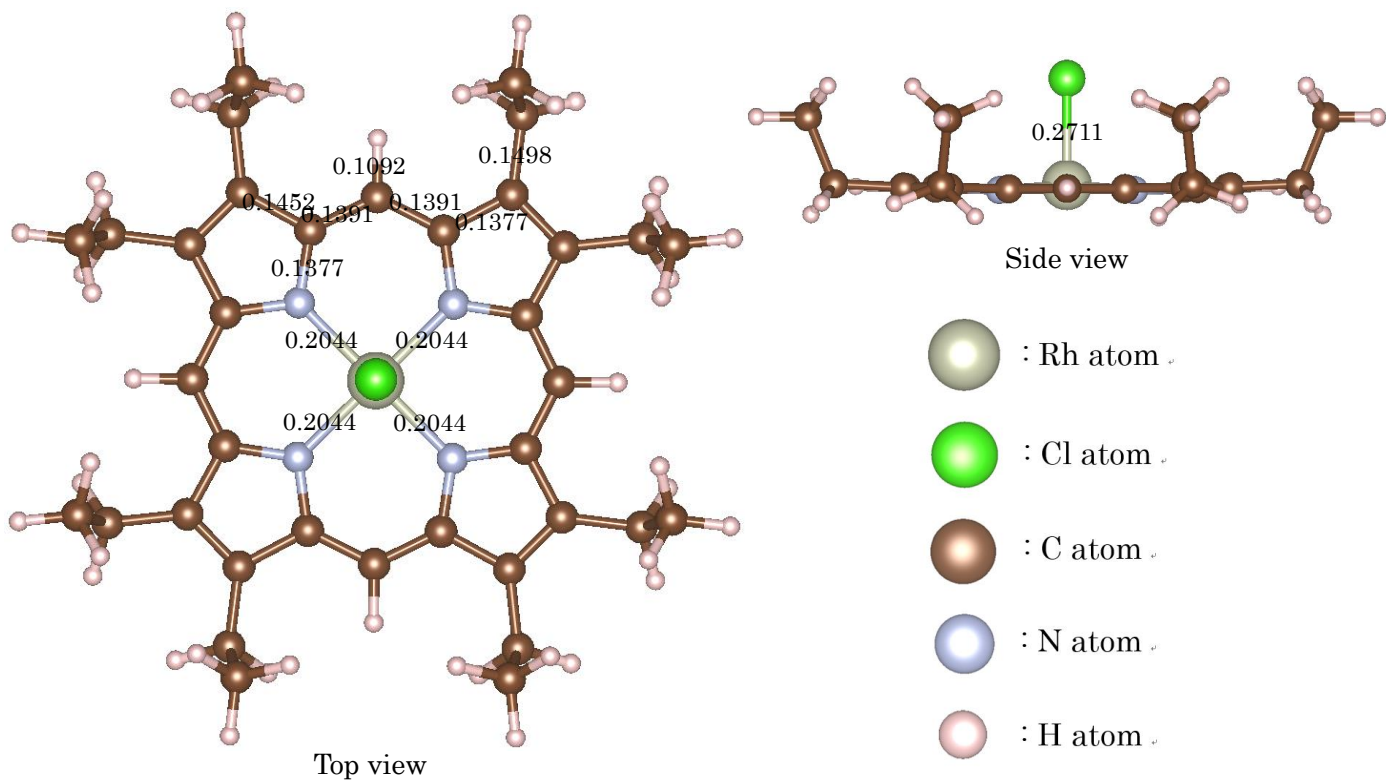
Fig. S9 The optimized geometry of [Rh^{III}(OEP)(Cl)] by PBE/PAW. The unit of length is nm.
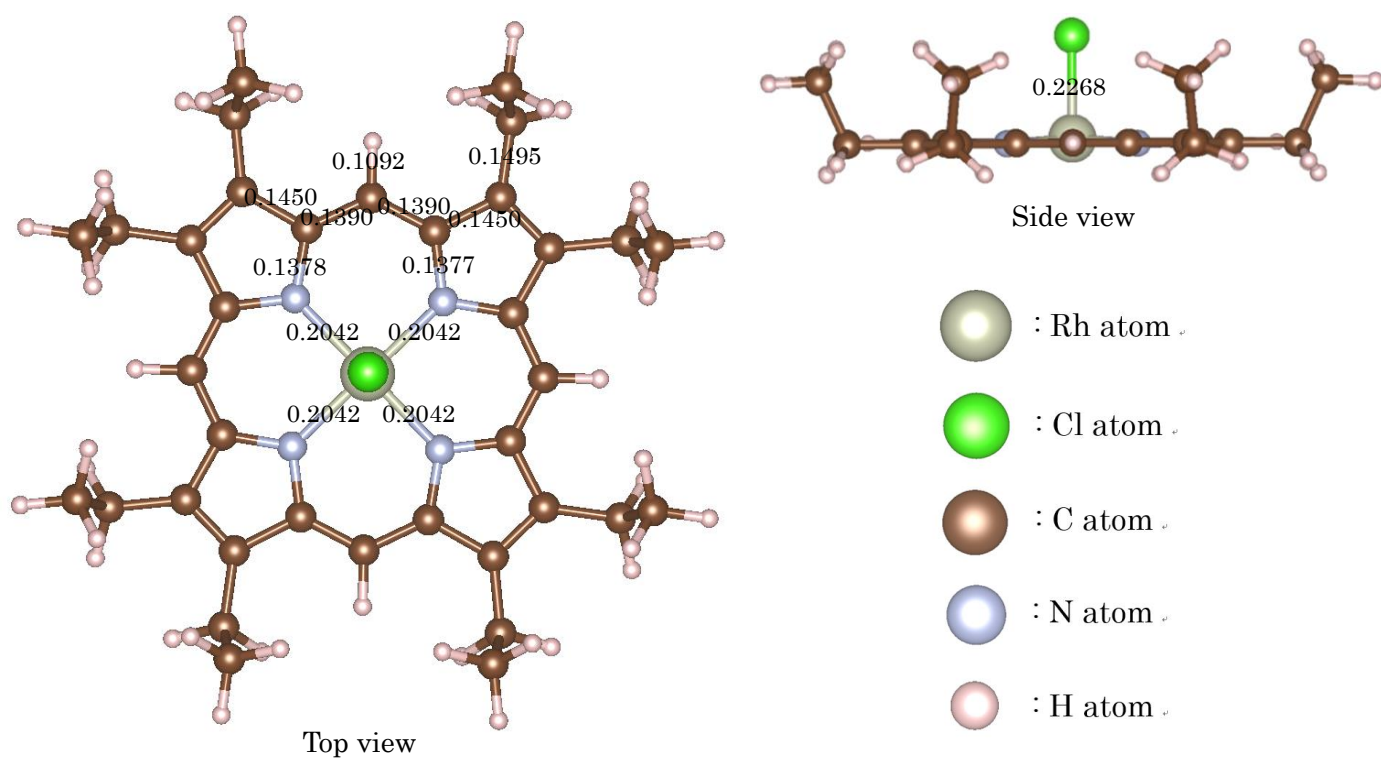
Fig. S10 The optimized geometry of [Rh^{III}(OEP)(Cl)] by PBE-D2/PAW. The unit of length is nm.

Top view

Side view

: Rh atom

: Cl atom

: C atom

: N atom

: H atom
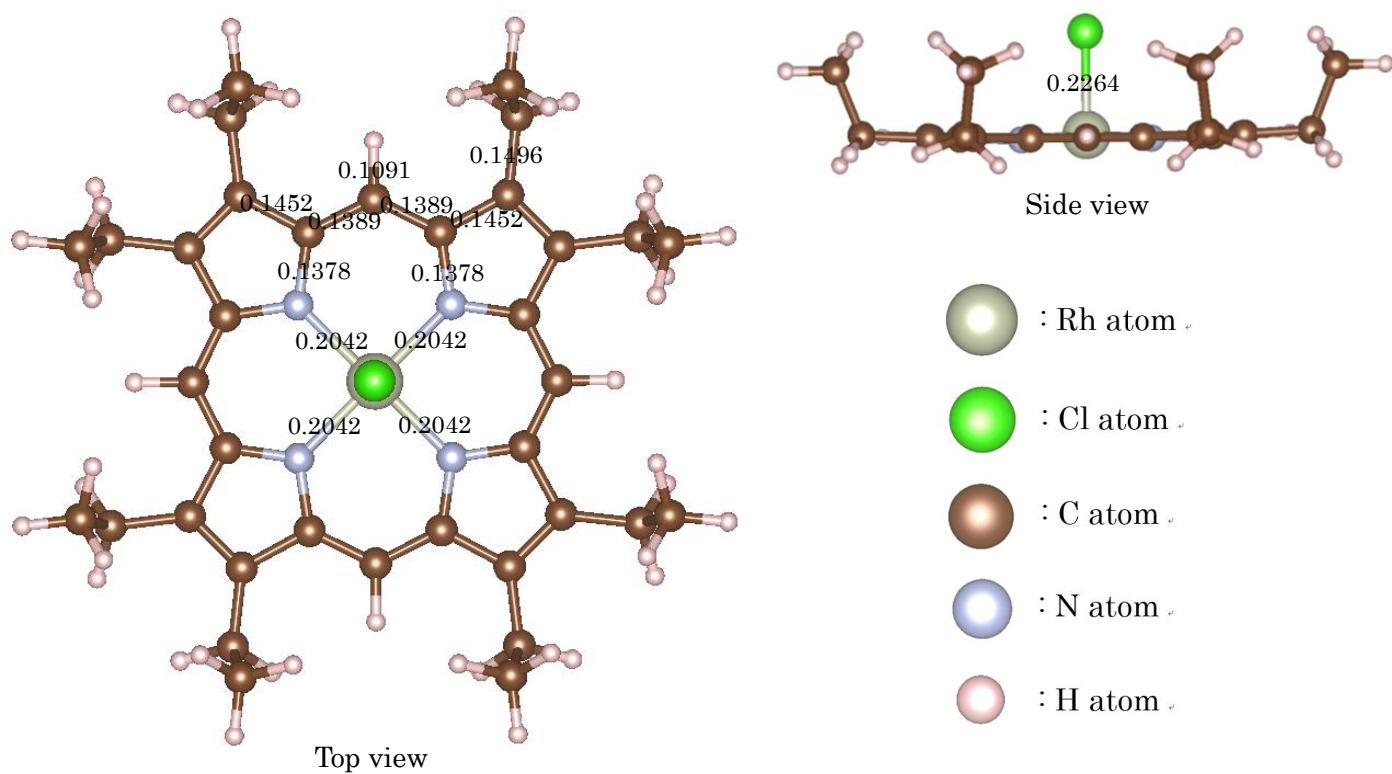
Fig. S11 The optimized geometry of [Rh^{III}(OEP)(Cl)] by PBE-D3/PAW. The unit of length is nm.

(a)   (b)
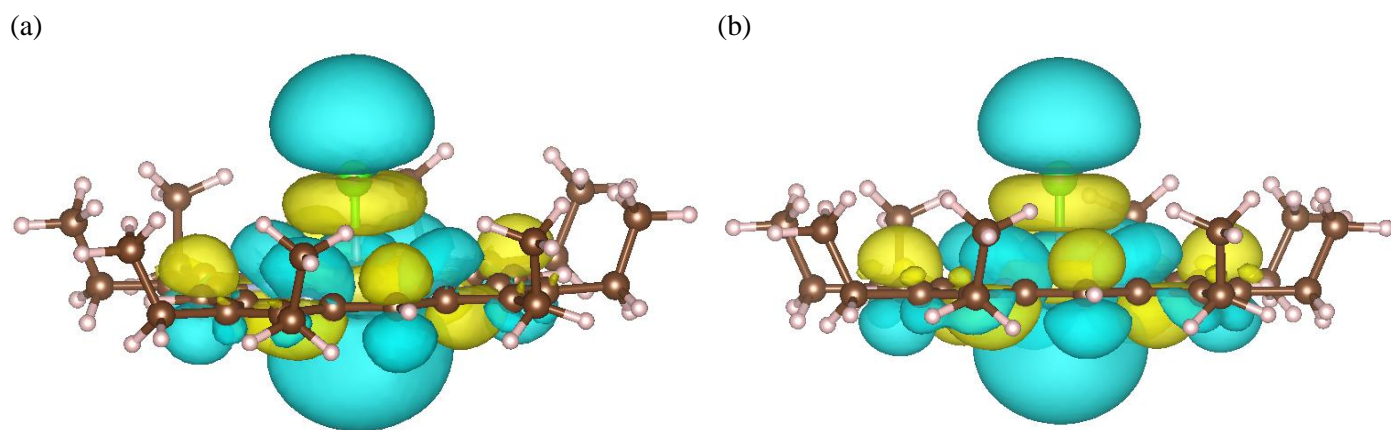
Fig. S12 The LUMOs of [Rh^{III}(OEP)(Cl)] calculated by (a) hybrid-DFT/SDD (for Rh), 6-31G(d) (for C), and 6-31+G(d,p) (for others), and (b) DFT-D2/PAW methods.

Results for the adsorption of [Rh^{III}(OEP)(Cl)] onto a two-layer graphite slab model

To investigate the effect of the number of layers of a graphite slab model on the results of [Rh^{III}(OEP)(Cl)] adsorbed onto a graphite basal surface calculated by DFT-D2 method [S24] with PBE exchange-correlation functional [S4], the most stable structure of the [Rh^{III}(OEP)(Cl)] adsorbed onto a two-layer graphite slab model was calculated. The distance between graphite sheets was set to 3.55 Å and the position of C atoms in graphite was kept fixed during geometry optimization for mimicking the bulk structure. The VASP [S22] program package was used for DFT calculations, and the VESTA [S26] program was used for visualization of calculation results.

The most stable structure of [Rh^{III}(OEP)(Cl)]/two-layer graphite is shown in Fig. S13, which also shows the geometry variations around the Rh^{III} center (Δd_2: Rh–Cl distance; Δd_3: Rh–N distance; and ΔA: N–Rh–N angle), the distance between [Rh^{III}(OEP)(Cl)] and graphite (d_1), adsorption energy (E_{ads}), chemical interaction energy (E^{int}_{chem}), such as for interactions involving orbital overlap and charge transfer, and the physical interaction energy (E^{in}_{tphys}), such as London forces (dispersion forces). E^{int}_{chem} and E^{int}_{phys} were estimated by equations (3) and (4) reported in the main text. Negative values correspond to stabilization. The results obtained for the [Rh^{III}(OEP)(Cl)]/two-layer graphite system are very similar to those obtained for [Rh^{III}(OEP)(Cl)]/single-layer graphite.

$d = 0.556$ nm

$d_1 = 0.330$ nm

Side view

Top view

$\Delta d_2 = -0.0006$ nm, $\Delta d_3 = -0.0004$ nm
ΔA(N-Rh-N) $= +1.6°$, $E_{ads} = -2.79$ eV
$E_{int}^{chem} = 1.02$ eV, $E_{int}^{phys} = -3.81$ eV
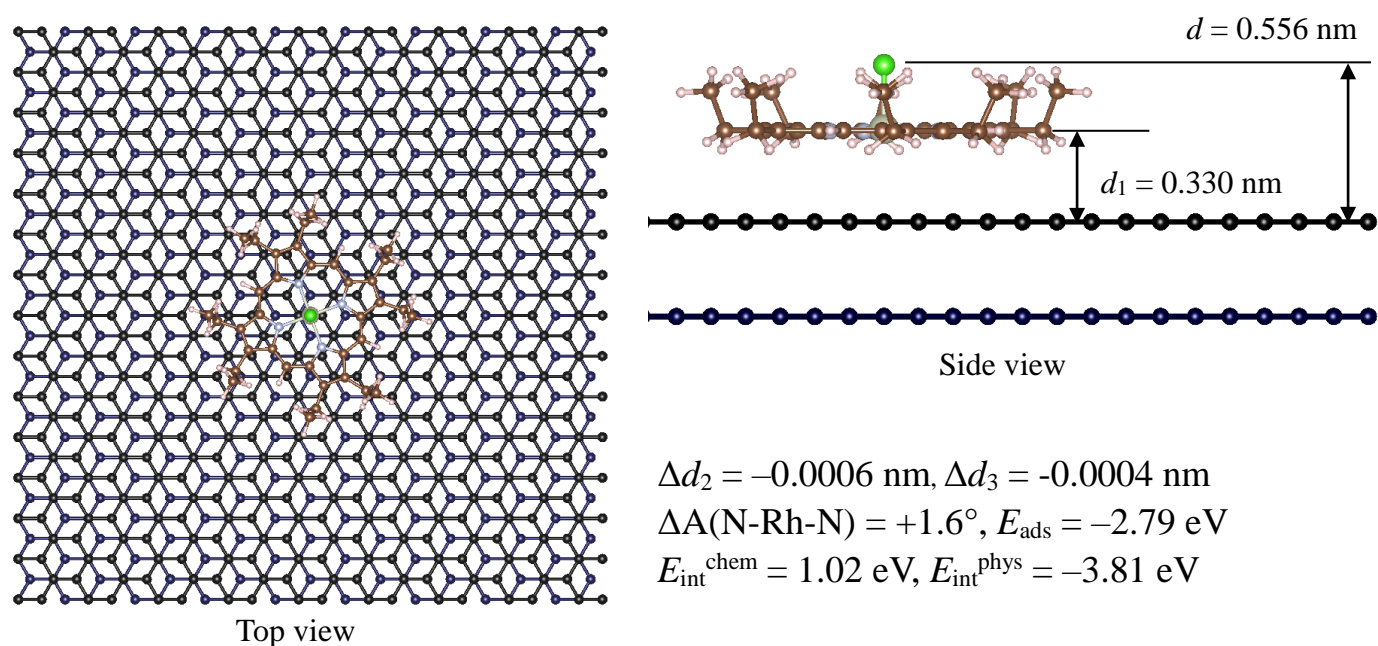
Fig. S13. Most stable structure of [Rh^{III}(OEP)(Cl)]/two-layer graphite model including the geometry variations around Rh^{III} (Δd_2: Rh–Cl distance; Δd_3: Rh–N distance; and ΔA: N–Rh–N angle), the distance between [Rh^{III}(OEP)(Cl)] and graphite (d_1), adsorption energy (E_{ads}), chemical interaction energy (E^{int}_{chem}), and physical interaction energy (E^{in}_{tphys}). E^{int}_{chem} and E^{int}_{phys} were estimated by equations (3) and (4) reported in the main text.

Results for the [Rh^{III}(OEP)(Cl)]/graphite system obtained by DFT-D3 method

DFT-D3 method [S25] is an improved method of DFT-D2 [S24], the method is more suitable than DFT-D2 in general. Although it is difficult that all structures are re-calculated by DFT-D3, we re-calculated the most stable structure of [Rh^{III}(OEP)(Cl)]/graphite system. The calculation result was summarized in Figure S14, and the result is same as that by DFT-D2, which is shown and discussed in main text.

$d = 0.569$ nm

$d_1 = 0.342$ nm

Side view

Top view

$\Delta d_2 = -0.0002$ nm, $\Delta d_3 = -0.0001$ nm
$\Delta A(\text{N-Rh-N}) = +0.8°$, $E_{ads} = -2.43$ eV
$E_{int}^{chem} = 0.42$ eV, $E_{int}^{phys} = -2.85$ eV
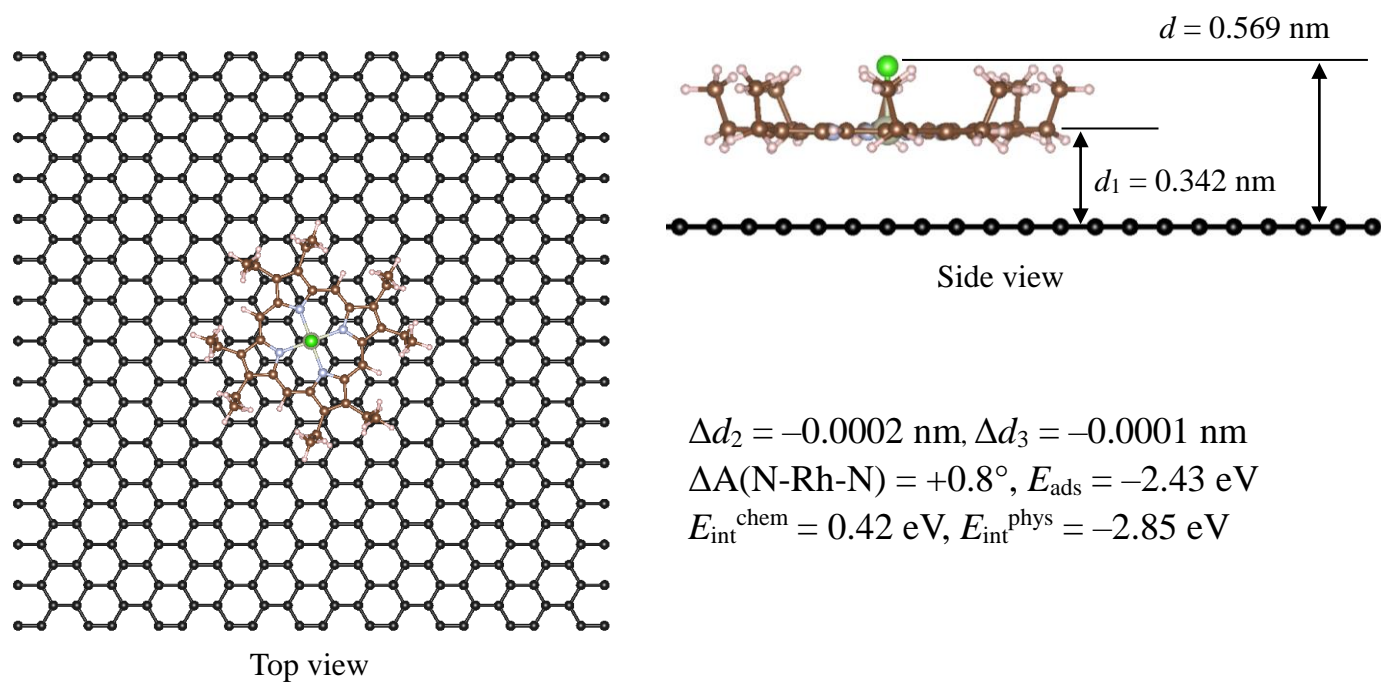
Fig. S14. Most stable structure of [Rh^{III}(OEP)(Cl)]/graphite model calculated by DFT-D3 method including the geometry variations around Rh^{III} (Δd_2: Rh–Cl distance; Δd_3: Rh–N distance; and ΔA: N–Rh–N angle), the distance between [Rh^{III}(OEP)(Cl)] and graphite (d_1), adsorption energy (E_{ads}), chemical interaction energy (E_{chem}^{int}), and physical interaction energy (E_{tphys}^{in}). E_{chem}^{int} and E_{phys}^{int} were estimated by equations (3) and (4) reported in the main text.

Results for the adsorption energies of the [Rh^{III}(OEP)(Cl)]/graphite basal surface system

      In the main text of the paper, we have shown only part of the results for the adsorption energies (E_{ads}) estimated by pure-DFT (GGA-PBE) and DFT-D (PBE-D2) methods. Here, we report all the results of E_{ads} for the calculated structures. In Figs. S15-S17, the results obtained by pure-DFT, while in Figs. S18-S20, those obtained by DFT-D, are reported. Using pure-DFT, we cannot obtain any negative value of E_{ads}, whereas, using the DFT-D method, we can obtain E_{ads} with negative values. However, even by using DFT-D, the value of E_{ads} becomes positive when the d_1 parameter (distance between the porphyrin ring and graphite basal surface) falls below 0.295 nm.
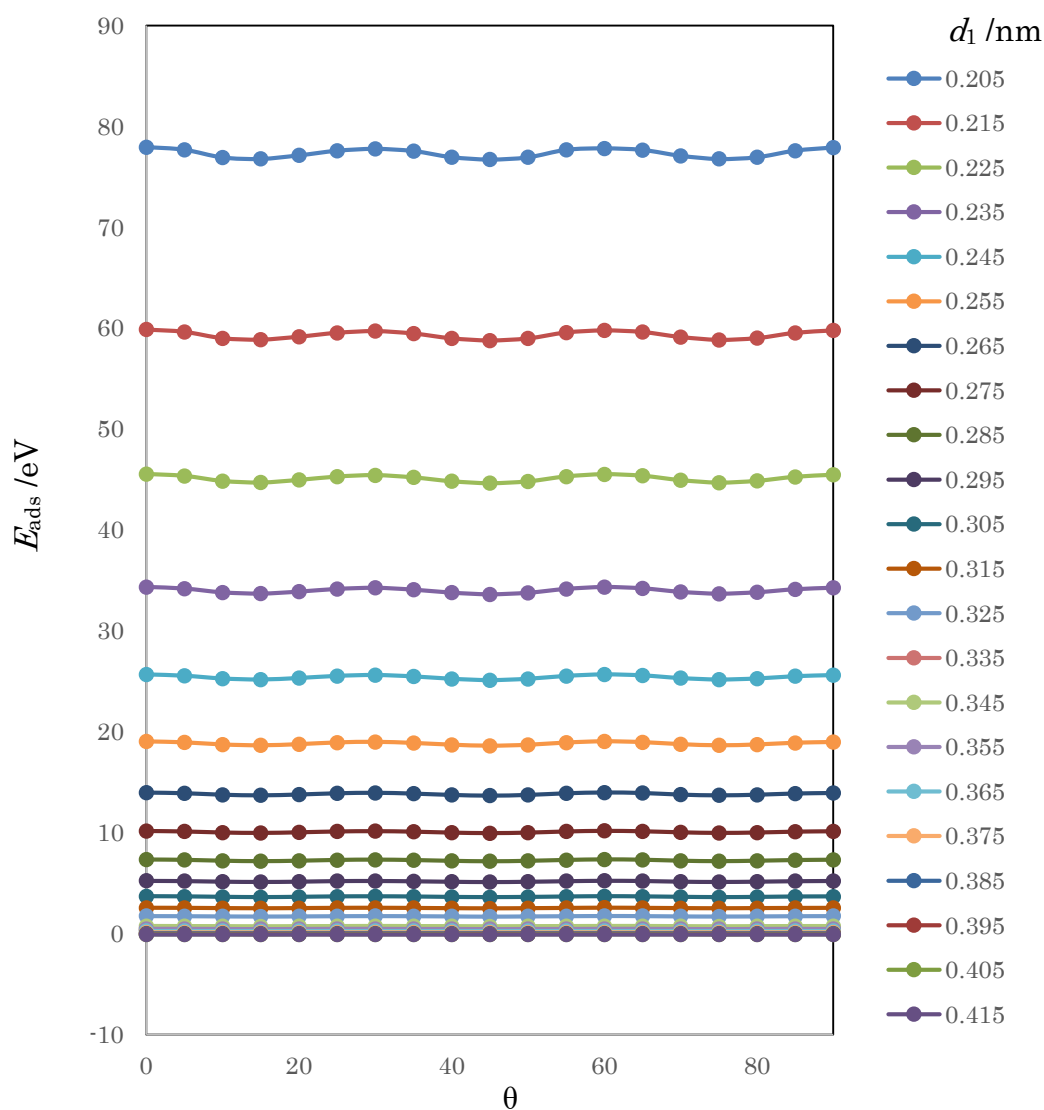
Fig. S15. Results of E_{ads} for on-top site adsorptions of [Rh^{III}(OEP)(Cl)] (the model shown in Fig. 5(b) in the main text) estimated by the pure-DFT (GGA-PBE) method.
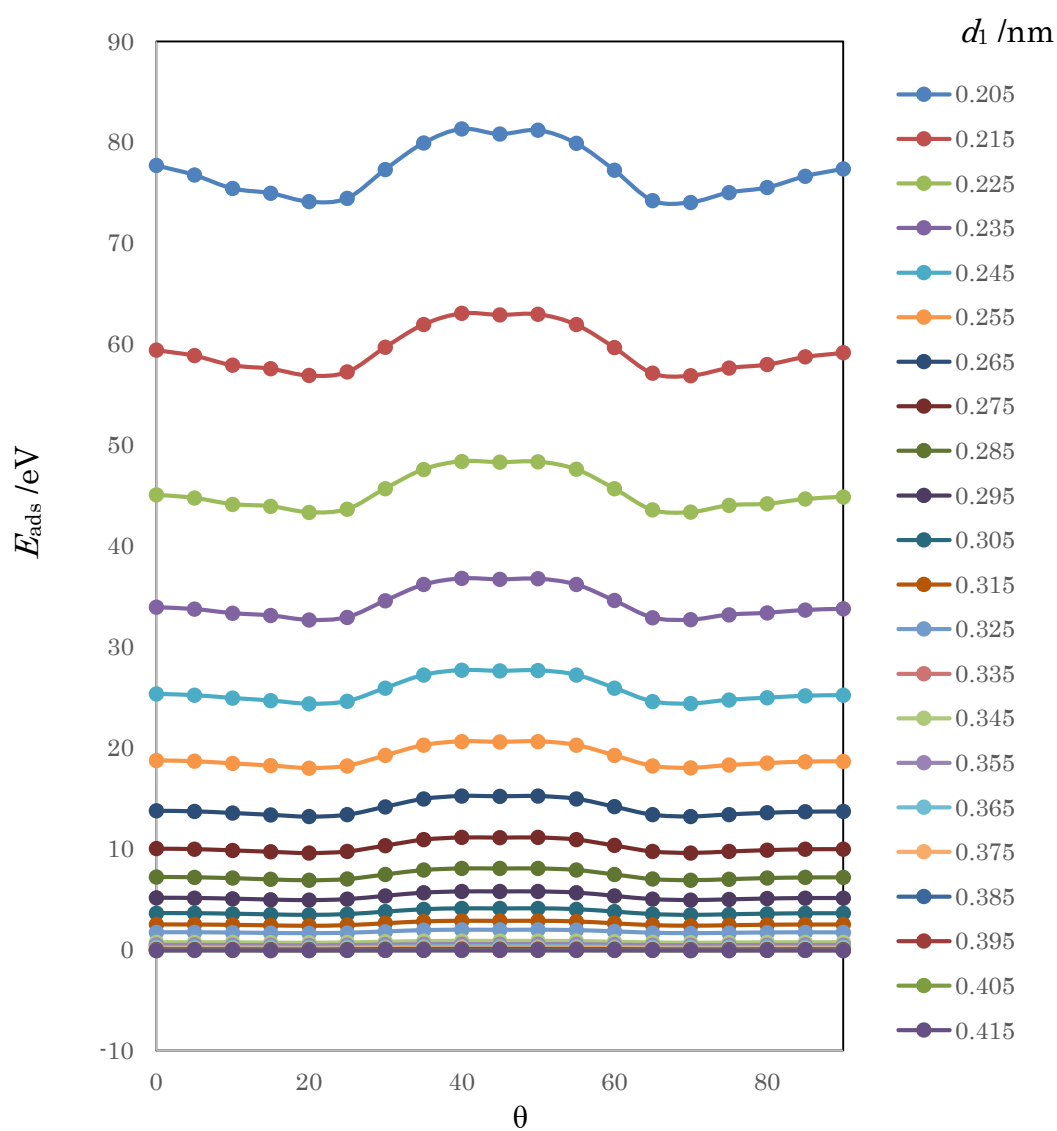
Fig. S16. Results of E_{ads} for bridge site adsorptions of [Rh^{III}(OEP)(Cl)] (model shown in Fig. 5(c) in the main text) estimated by the pure-DFT (GGA-PBE) method.
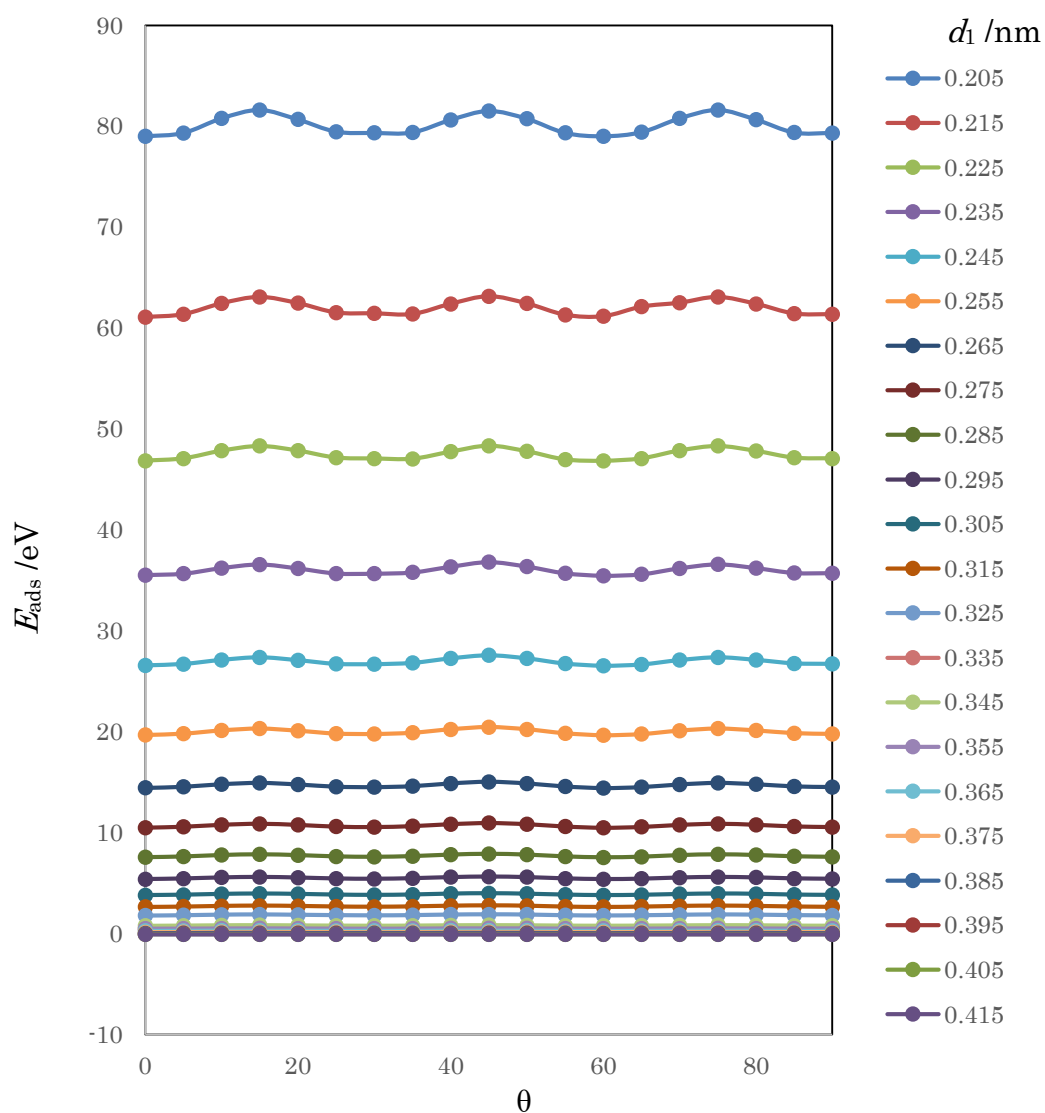
Fig. S17. Results of E_{ads} for hollow site adsorptions of [Rh^{III}(OEP)(Cl)] (model shown in Fig. 5(d) in the main text) estimated by the pure-DFT (GGA-PBE) method.
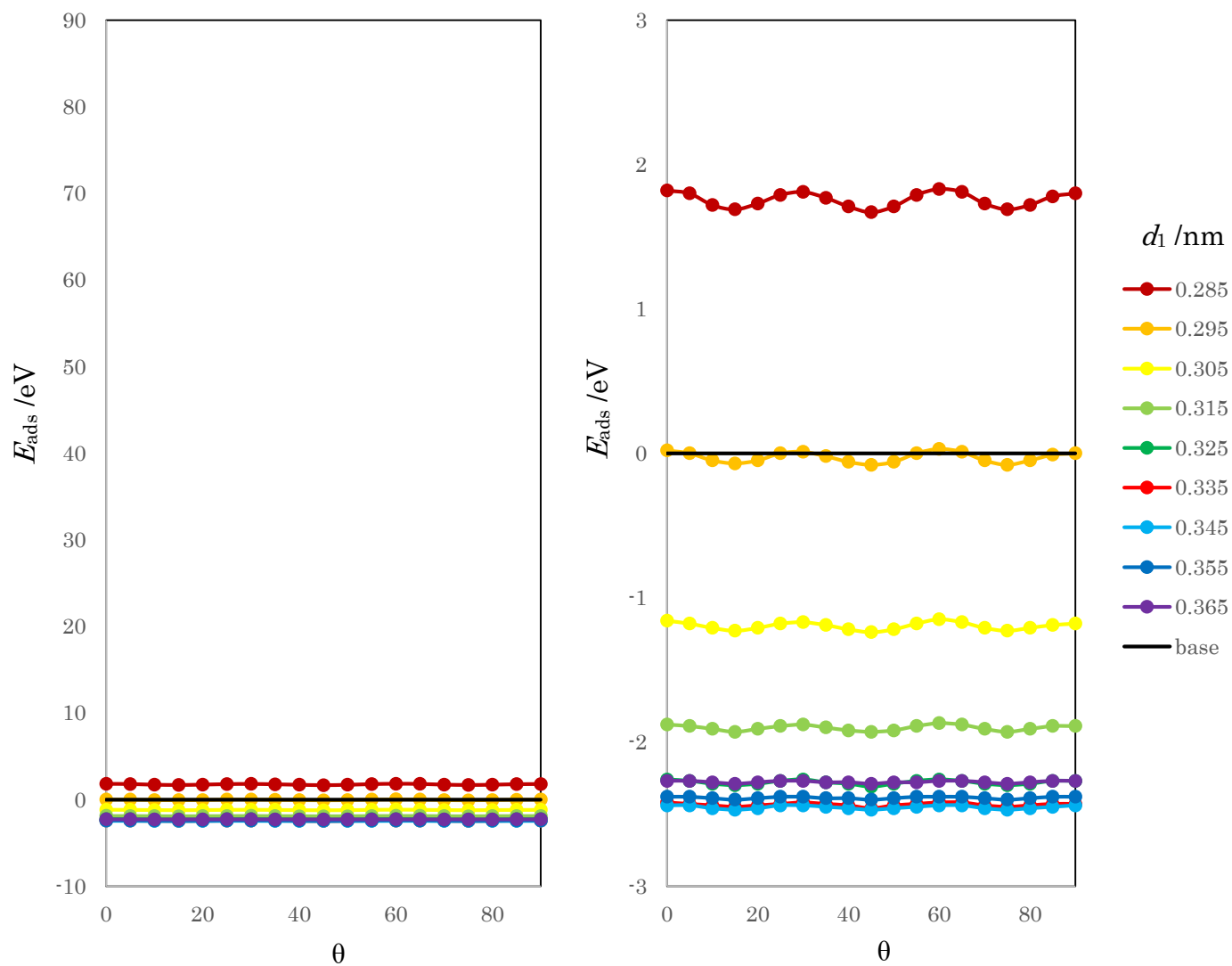
Fig. S18. Results of E_{ads} for on-top site adsorptions of [Rh^{III}(OEP)(Cl)] (model shown in Fig. 5(b) in the main text) estimated by DFT-D (PBE-D2) method. The left panel has the same magnification of E_{ads} as Figs. S9-S11, while the right panel shows an enlarged view.
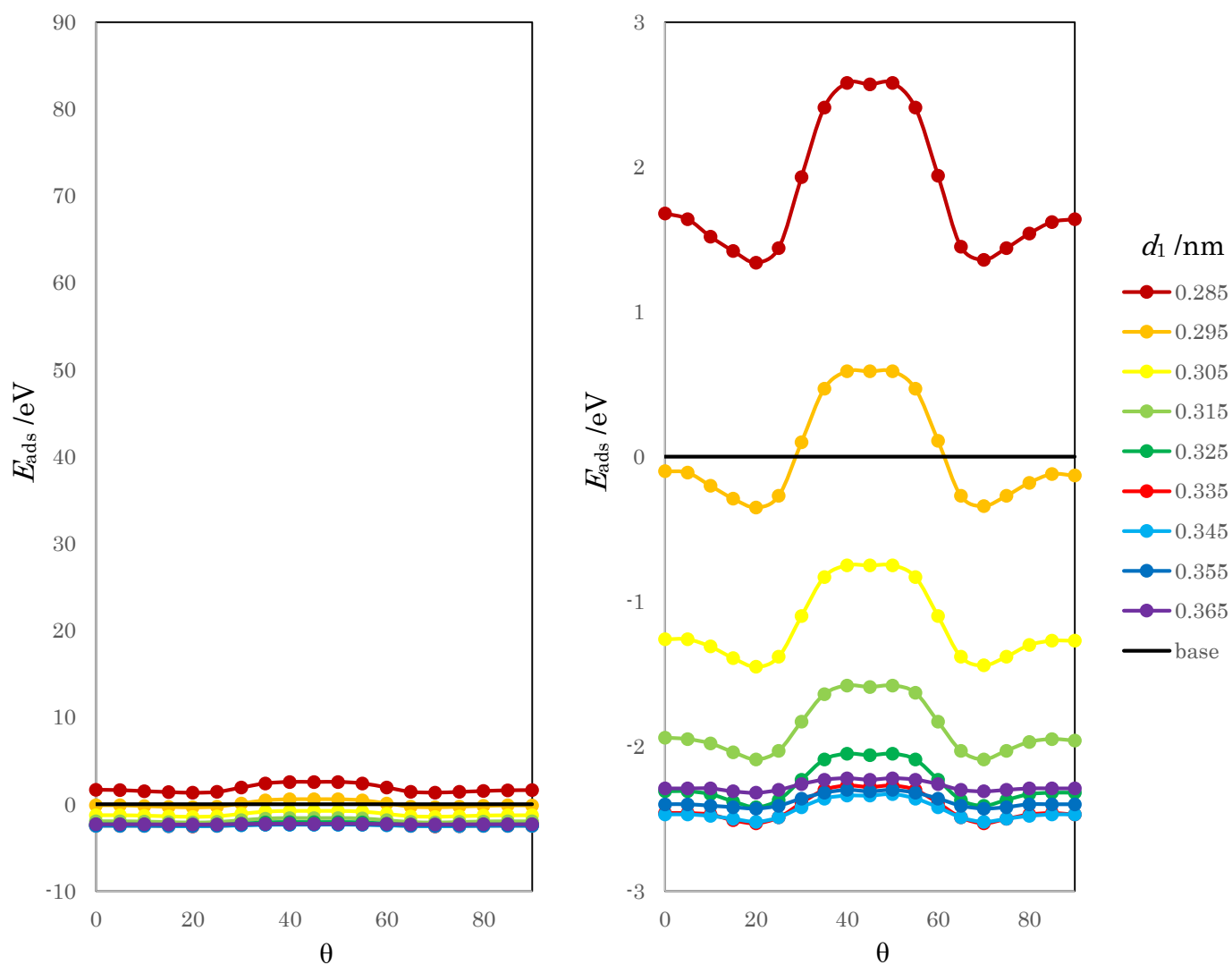
Fig. S19. Results of E_{ads} for bridge site adsorptions of [Rh^{III}(OEP)(Cl)] (model shown in Fig. 5(c) in the main text) estimated by the DFT-D (PBE-D2) method. The left panel has the same magnification of E_{ads} as Figs. S9-S11, while the right panel shows an enlarged view.
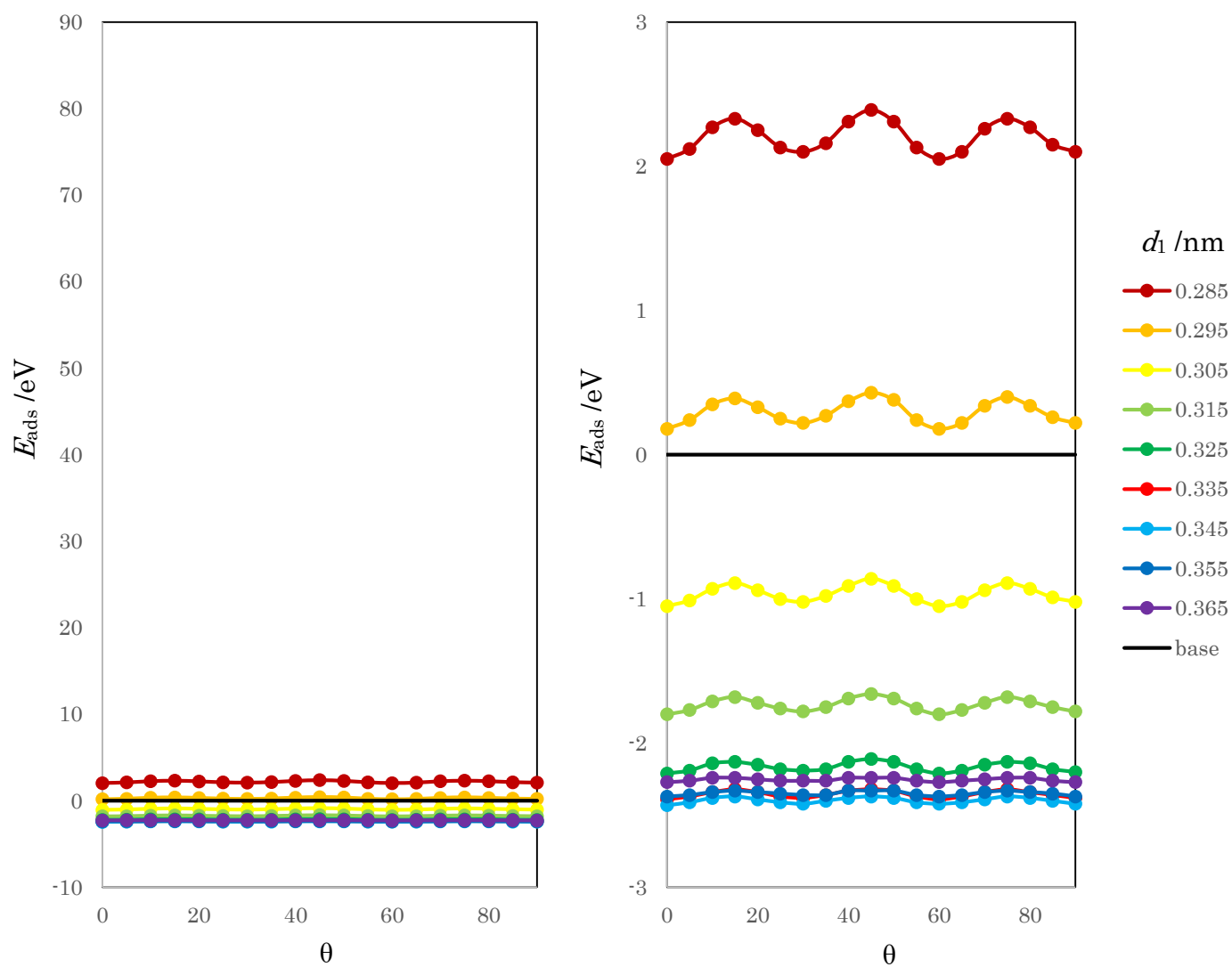
Fig. S20. Results of E_{ads} of bridge site adsorptions of [Rh^{III}(OEP)(Cl)] (model shown in Fig. 5(d) in the main text) estimated by the DFT-D (PBE-D2) method. The left panel has the same magnification of E_{ads} as Figs. S9-S11, while the right panel shows an enlarged view.

Results for height profiles of molecular layers on HOPG observed by AFM

To ensure that the molecular layers of [Rh^{III}(OEP)(Cl)] on HOPG observed in Fig. 9 in the main text are the same as those reported in our recent work [S27], we investigated the height profile of the molecular layers such as the monolayer sheet and aggregated layer. As shown in Fig. S21, the height profile of the monolayer and aggregated layer are 0.44 nm and 1.21 nm, respectively. These results are consistent with our recent results [S27].

(a)

(c)

(d)
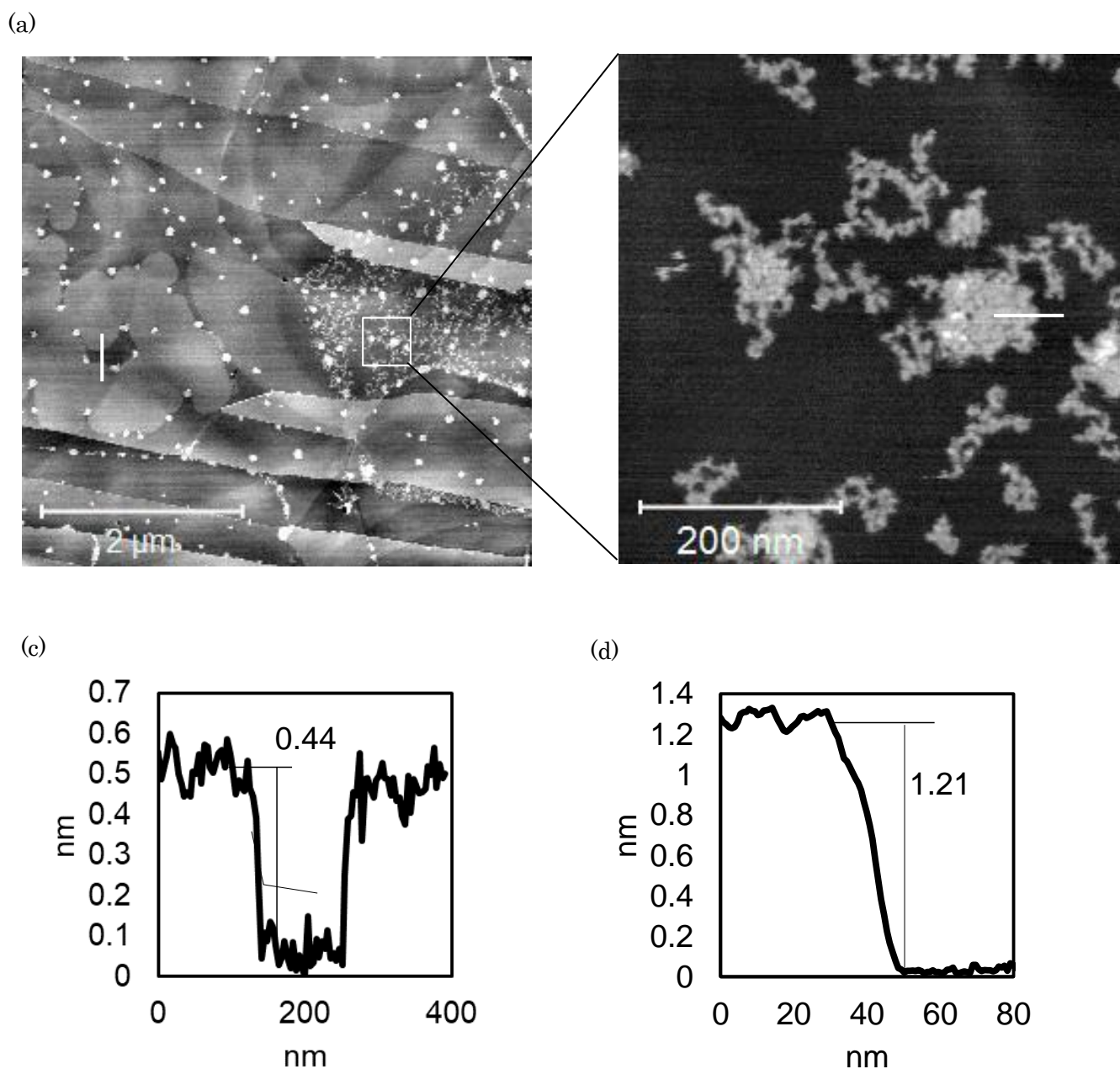
Fig. S21. (a) AFM image of [Rh^{III}(OEP)(Cl)]/HOPG (identical to Fig. 9(a) in the main text), (b) enlarged AFM image of the square area in (a), (c) height profile along the white line drawn in (a) that corresponds to the height profile of a monolayer sheet of [Rh^{III}(OEP)(Cl)], and (d) height profile along the white line drawn in (b) that corresponds to the height profile of an aggregated layer of [Rh^{III}(OEP)(Cl)].

Results for the frontier orbitals of the [Rh^{III}(OEP)(Cl)]/graphite basal surface system

Here, we show the results obtained for the frontier orbitals of the most stable [Rh^{III}(OEP)(Cl)]/graphite basal surface model estimated by the DFT-D method. For calculations, the Advance/PHASE program package was used.
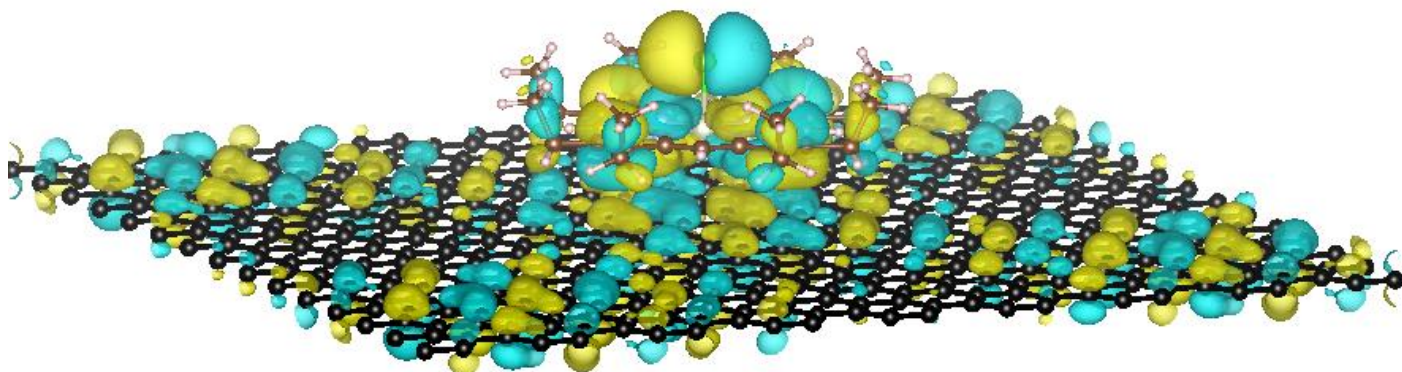
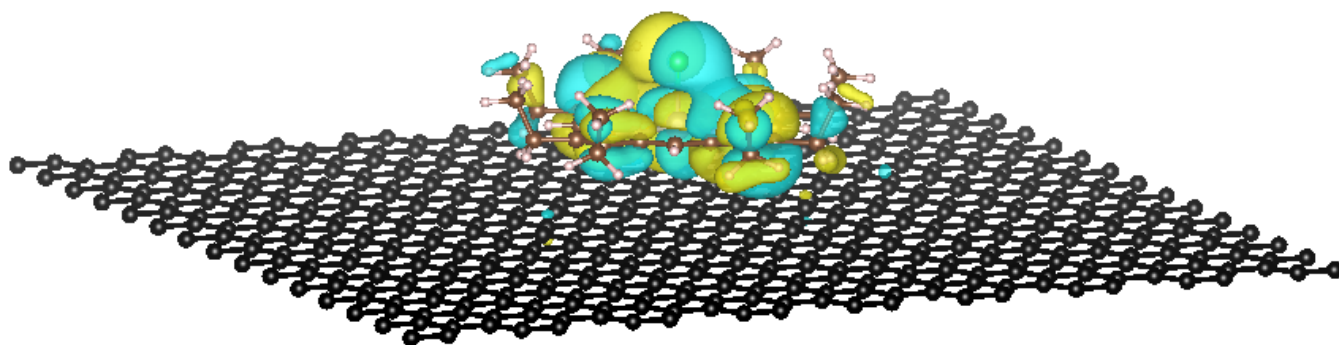

Fig. S22. HOMO–12 of the most stable [Rh^{III}(OEP)(Cl)]/graphite system. The isosurface value is 0.01 a.u..
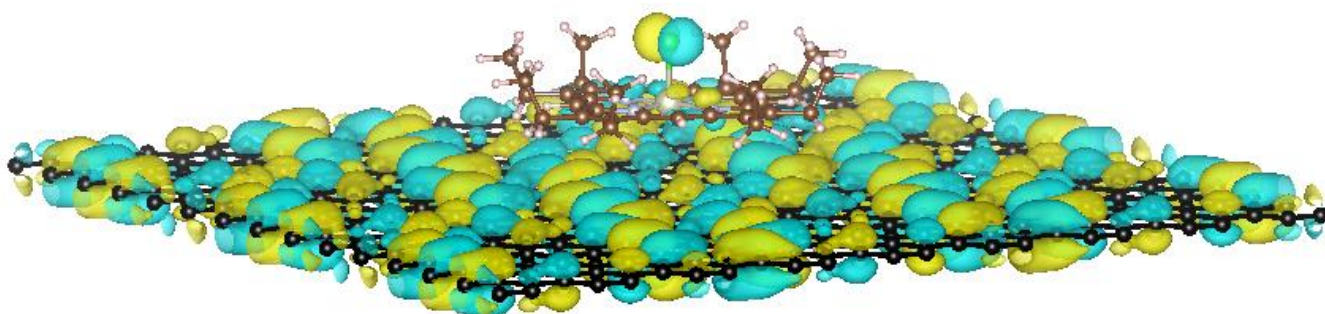
Fig. S23. HOMO–11 of the most stable [Rh^{III}(OEP)(Cl)]/graphite system. The isosurface value is 0.01 a.u..
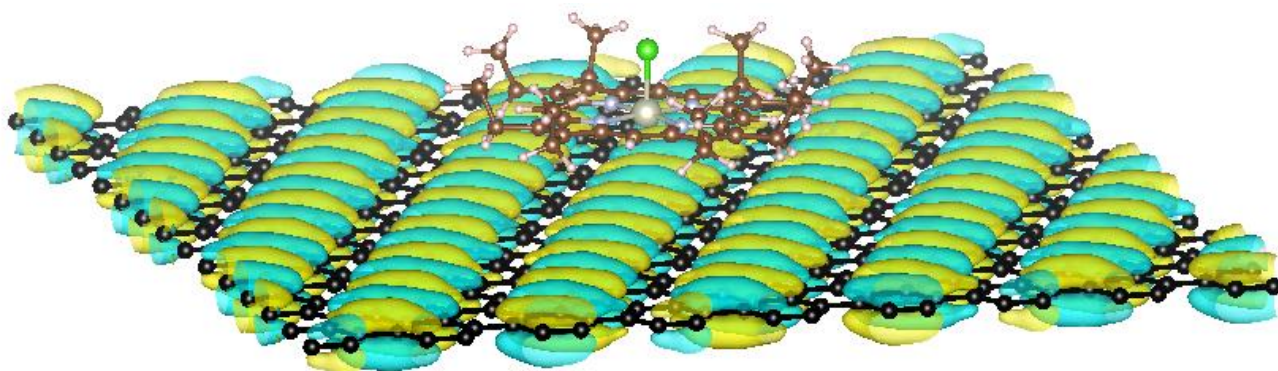
Fig. S24. HOMO–10 of the most stable [Rh^{III}(OEP)(Cl)]/graphite system. The isosurface value is 0.01 a.u..
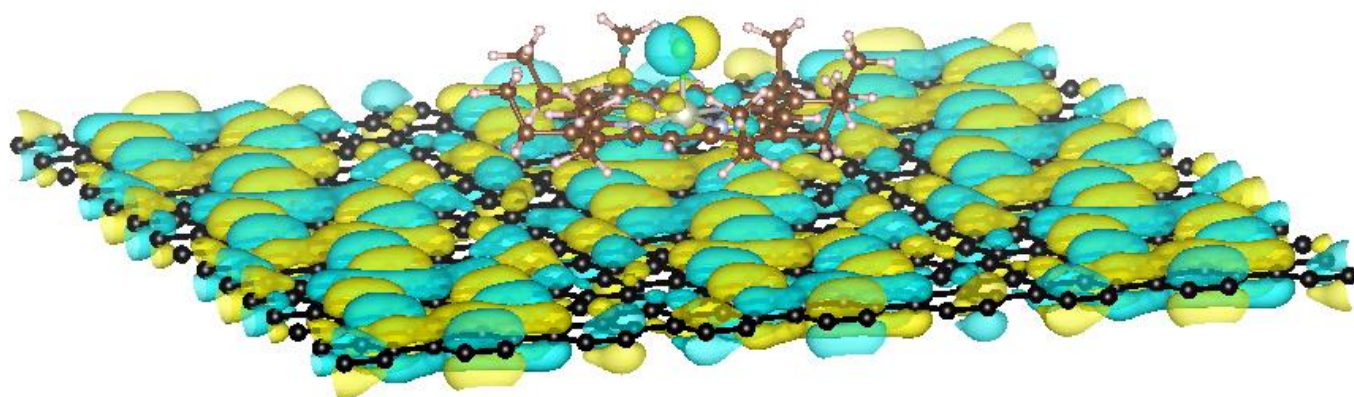
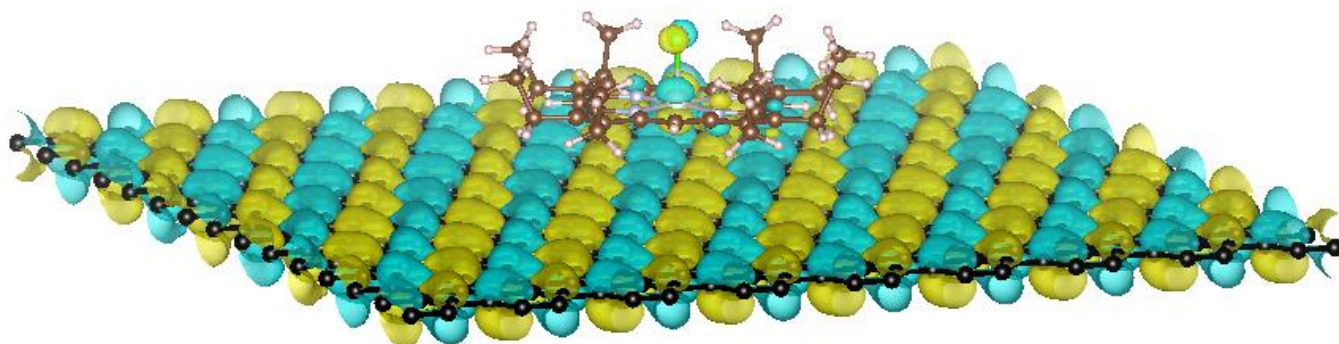Fig. S25. HOMO–9 of the most stable [Rh^{III}(OEP)(Cl)]/graphite system. The isosurface value is 0.01 a.u..
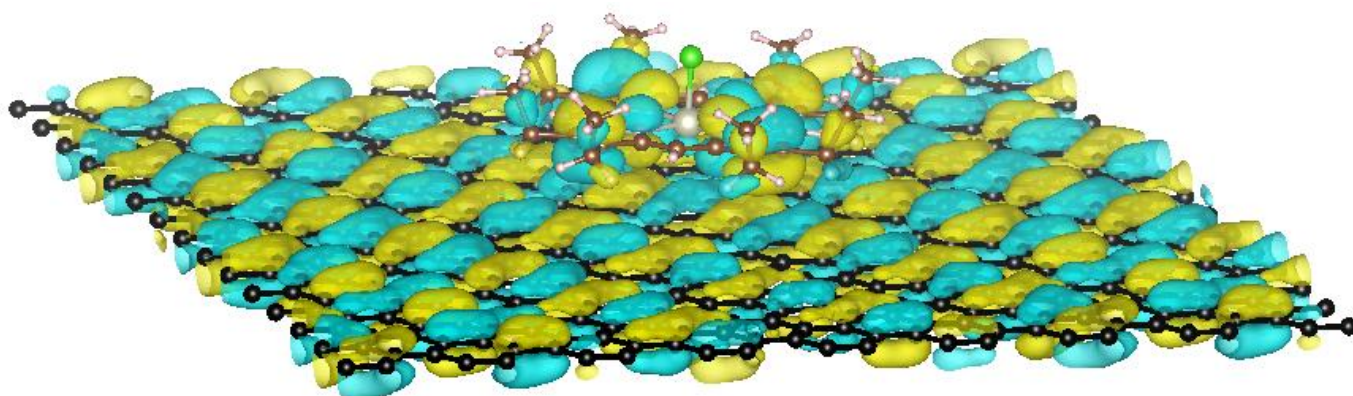
Fig. S26. HOMO–8 of the most stable [Rh^{III}(OEP)(Cl)]/graphite system. The isosurface value is 0.01 a.u..
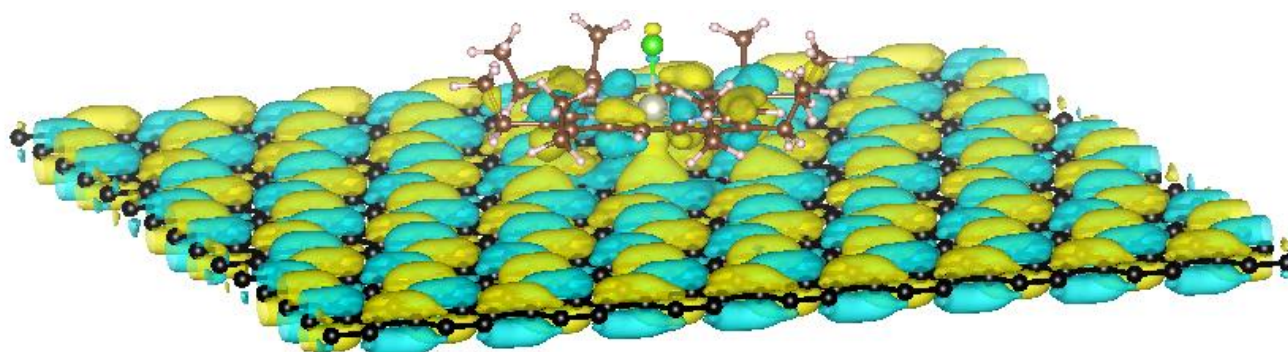
Fig. S27. HOMO–7 of the most stable [Rh^{III}(OEP)(Cl)]/graphite system. The isosurface value is 0.01 a.u..
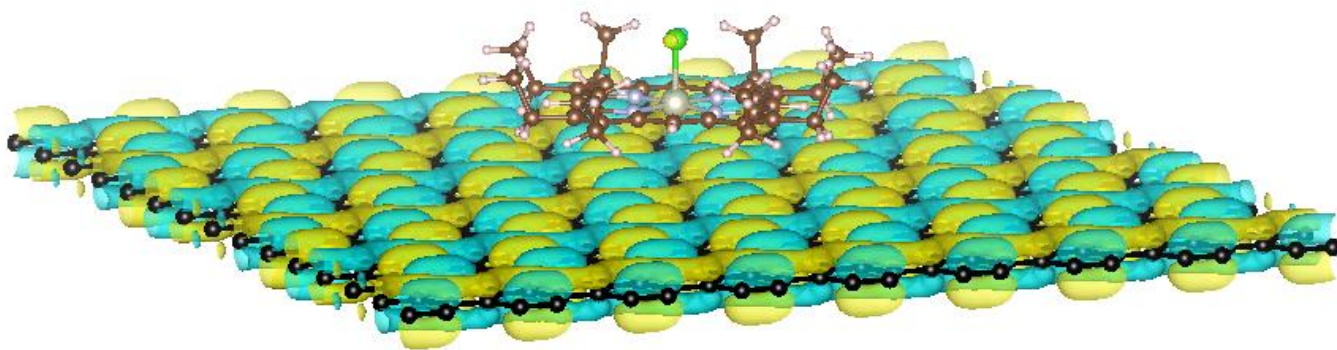
Fig. S28. HOMO–6 of the most stable [Rh^{III}(OEP)(Cl)]/graphite system. The isosurface value is 0.01 a.u..
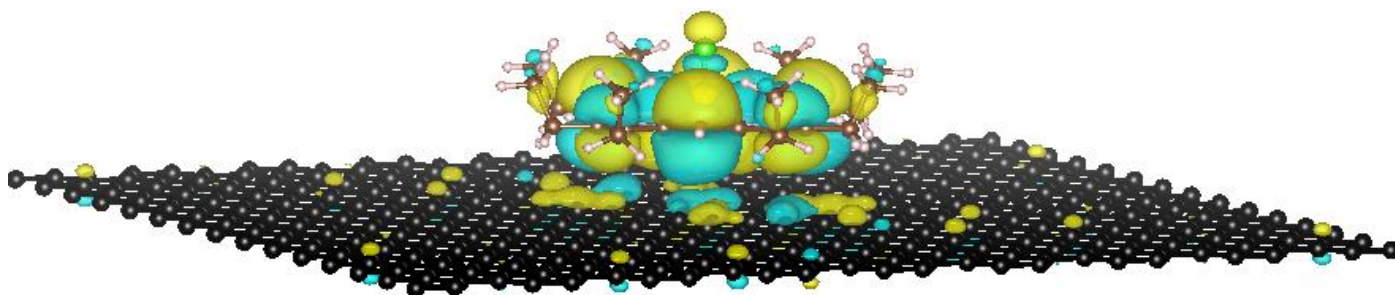
Fig. S29. HOMO–5 of the most stable [Rh^{III}(OEP)(Cl)]/graphite system. The isosurface value is 0.01 a.u..
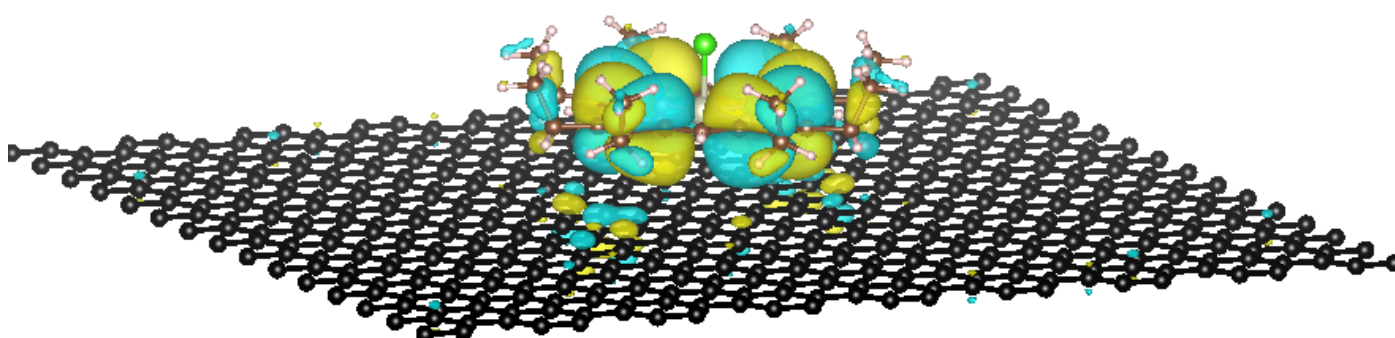
Fig. S30. HOMO–4 of the most stable [Rh^{III}(OEP)(Cl)]/graphite system. The isosurface value is 0.01 a.u..
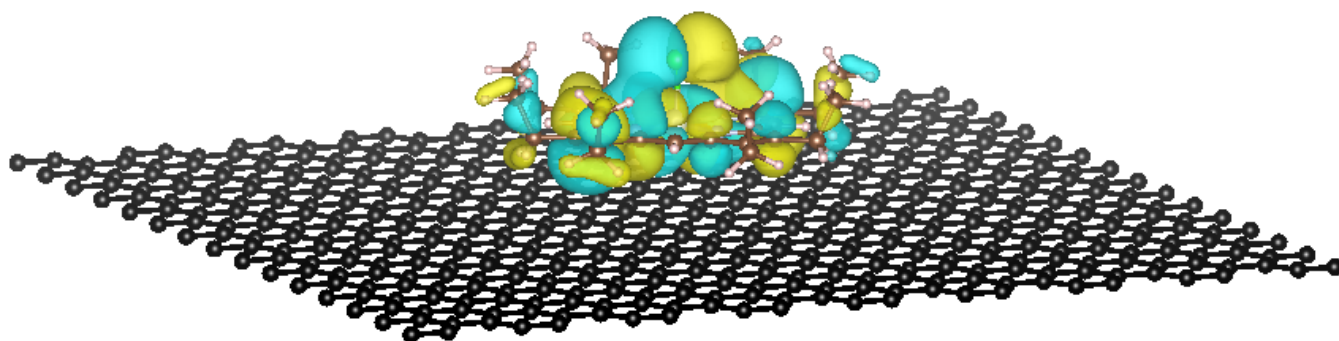
Fig. S31. HOMO–3 of the most stable [Rh^{III}(OEP)(Cl)]/graphite system. The isosurface value is 0.01 a.u..

Fig. S32. HOMO–2 of the most stable [Rh^{III}(OEP)(Cl)]/graphite system. The isosurface value is 0.01 a.u..

Fig. S33. HOMO–1 of the most stable [Rh^{III}(OEP)(Cl)]/graphite system. The isosurface value is 0.01 a.u..
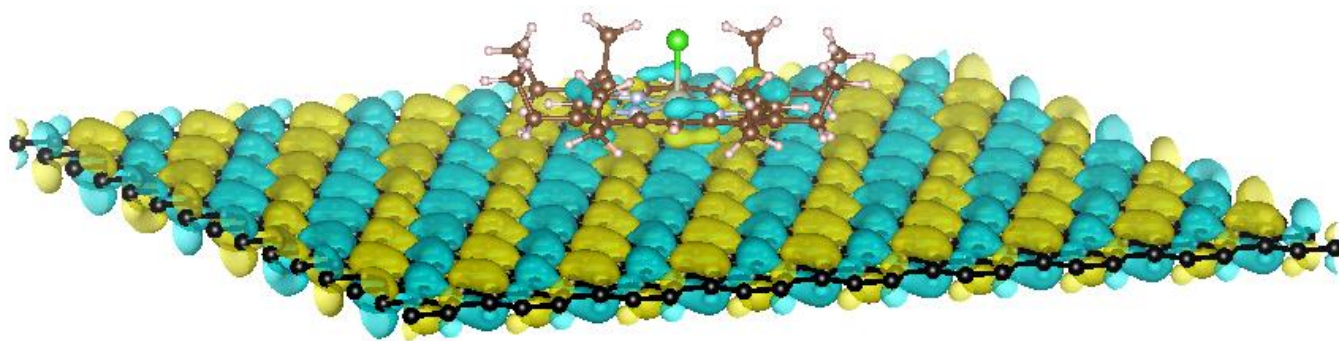
Fig. S34. HOMO of the most stable [Rh^{III}(OEP)(Cl)]/graphite system. The isosurface value is 0.01 a.u..
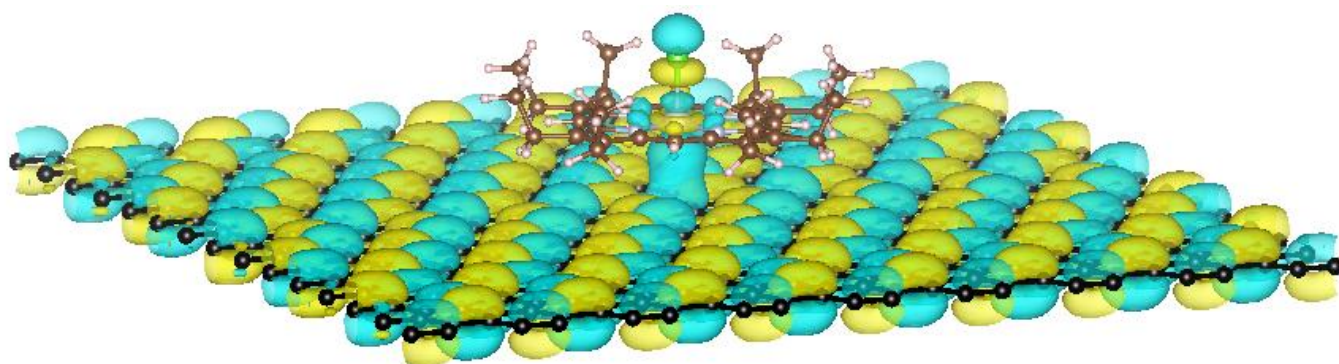
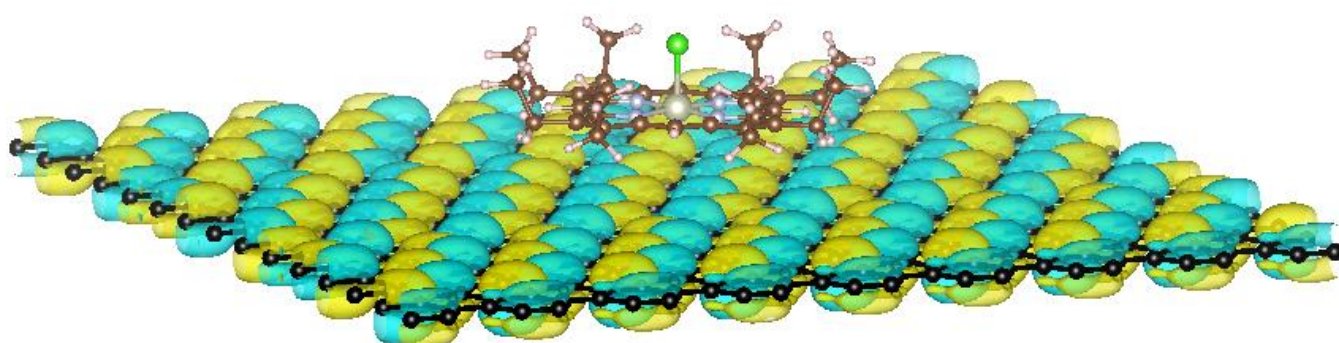Fig. S35. LUMO of the most stable [Rh^{III}(OEP)(Cl)]/graphite system. The isosurface value is 0.01 a.u..

Fig. S36. LUMO+1 of the most stable [Rh^{III}(OEP)(Cl)]/graphite system. The isosurface value is 0.01 a.u..
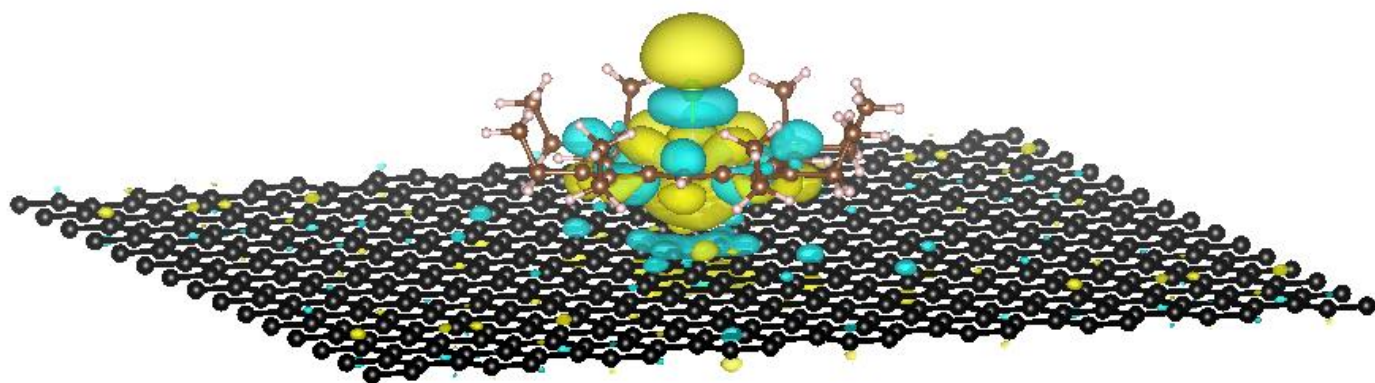
Fig. S37. LUMO+2 of the most stable [Rh^{III}(OEP)(Cl)]/graphite system. The isosurface value is 0.01 a.u..

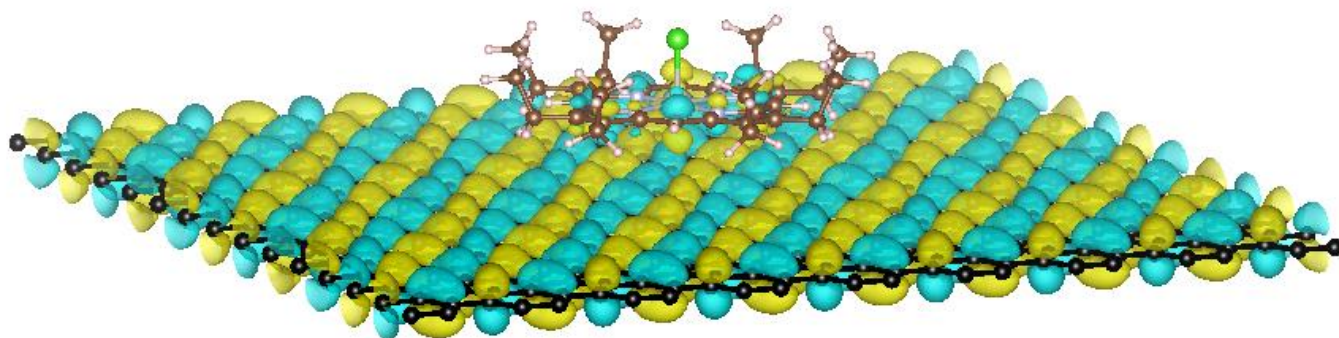Fig. S38. LUMO+3 of the most stable [Rh^{III}(OEP)(Cl)]/graphite system. The isosurface value is 0.01 a.u..
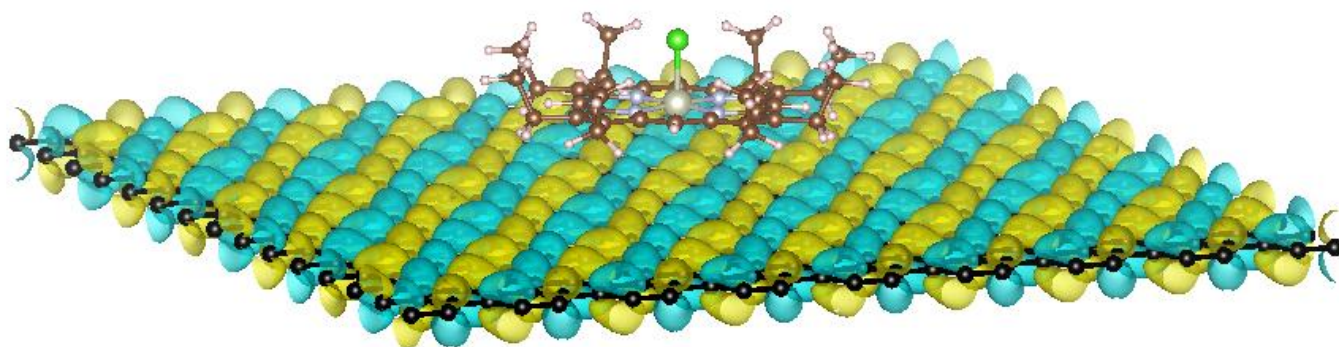

Fig. S39. LUMO+4 of the most stable [Rh^{III}(OEP)(Cl)]/graphite system. The isosurface value is 0.01 a.u..
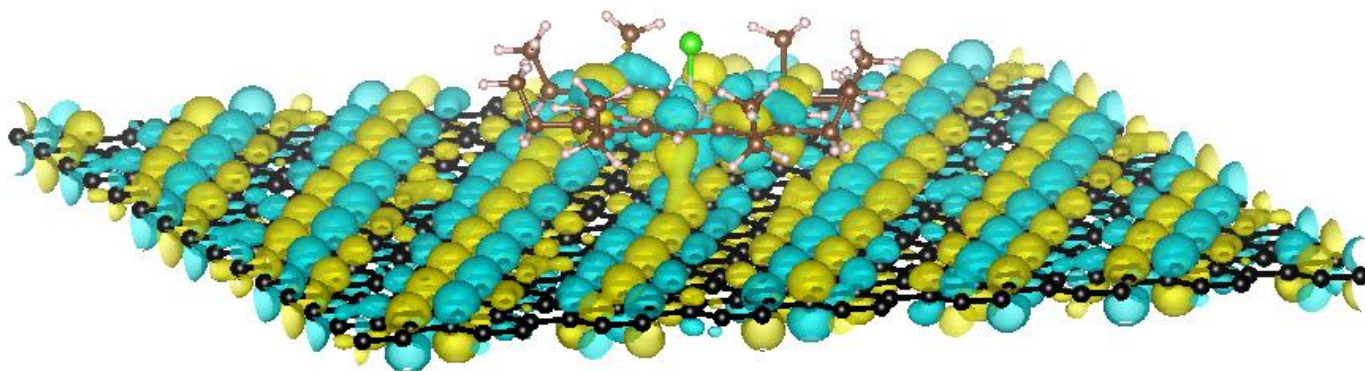
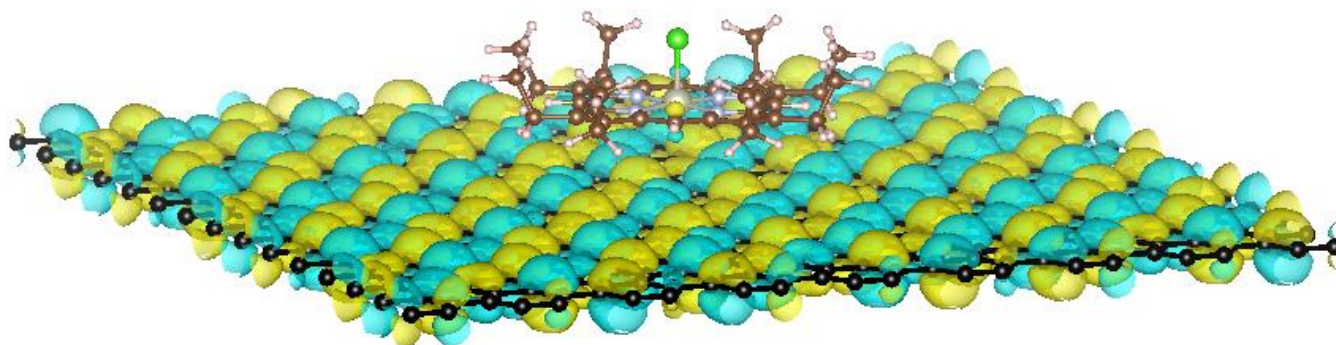Fig. S40. LUMO+5 of the most stable [Rh^{III}(OEP)(Cl)]/graphite system. The isosurface value is 0.01 a.u..

Fig. S41. LUMO+6 of the most stable [Rh^{III}(OEP)(Cl)]/graphite system. The isosurface value is 0.01 a.u..
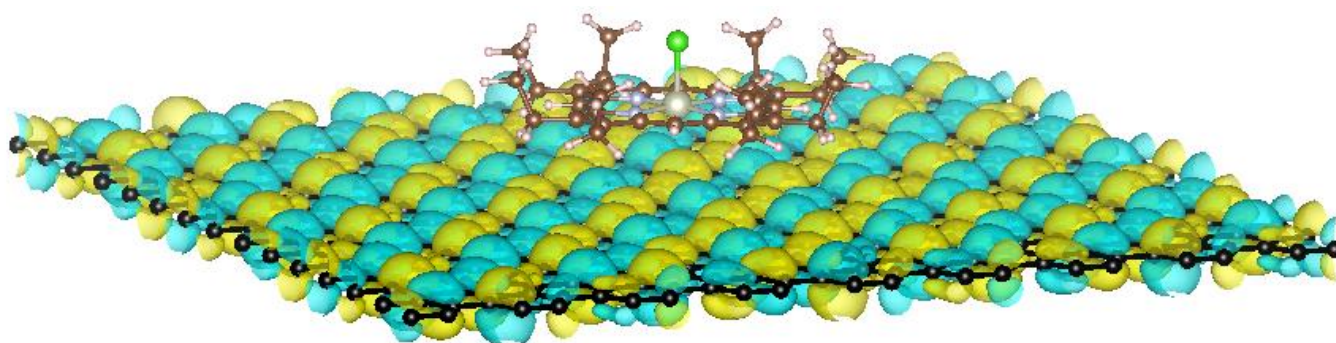
Fig. S42. LUMO+7 of the most stable [Rh^{III}(OEP)(Cl)]/graphite system. The isosurface value is 0.01 a.u..

References for supplementary material

[S1] a) K. Kowalski, P. Piecuch, Mol. Phys., 102 (2004) 2425; b) H. Paulsen, V. Schunemann, and J.A. Wolny, Eur. J. Inorg. Chem., (2013) 628; c) A. Szabo and N.S. Oatlund, Modern Quantum Chemistry, Dover (1996); d) C. Møller and M.S. Plesset, Phys. Rev., 46 (1934) 0618; e) R.J. Bartlet and G.D. Purvis III, Int. J. Quantum Chem., 14 (1978) 561; f) J. A. Pople, M. Head-Gordon, and K. Raghavachari, J. Chem. Phys., 87 (1987) 5968; g) H. Nakatsuji and K. Hirao, J. Chem. Phys., 68 (1978) 2053; h) K. Hallberg, Adv. Phys., 55 (2006) 477

[S2] W. Kohn and L.J. Sham, Phys. Rev., 140 (1965) A1133

[S3] a) A.D. Becke, Phys. Rev. A, 38 (1988) 3098; b) C. Lee, W. Yang, and R.G. Parr, Phys. Rev. B, 37 (1988) 785

[S4] a) J.P. Perdew, K. Burke, and M. Ernzerhof, Phys. Rev. Lett., 77 (1996) 3865; b) J.P. Perdew, K. Burke, and M. Ernzerhof, Phys. Rev. Lett., 78 (1997) 1396

[S5] a) A.D. Becke, J. Chem. Phys., 98 (1993) 5648; b) C. Lee, W. Yang, and R.G. Parr, Phys. Rev. B, 37, (1988) 785

[S6] a) J.P. Perdew and Y. Wang, Phys. Rev. B, 45, 13244; b) A.D. Becke, Phys. Rev. A, 38 (1988) 3098

[S7] C. Adamo and V. Barone, J. Chem. Phys., 110 (1999) 6158

[S8] Y. Zhao, N.E. Schultz, and D. G. Truhlar, J. Chem. Phys., 123 (2005) 161103

[S9] Y. Zhao and D. G. Truhlar, Theor. Chem. Acc., 120 (2008) 215

[S10] T. Yanai, D. Tew, and N. Handy, Chem. Phys. Lett., 393 (2004) 51

[S11] a) O.A. Vydrov and G. Scuseria, J. Chem. Phys., 125 (2006) 234109; b) O.A. Vydrov, J. Heyd, A. Krukou, and G. Scuseria, J. Chem. Phys., 125 (2006) 074106; c) O.A. Vydrov, G. Scuseria, and J. P. Perdew, J. Chem. Phys., 126 (2007) 154109

[S12] P. Schwerdfeger, M. Dolg, W.H.E. Schwarz, G.A. Bowrnaker, and P.D.W. Boyd, J. Chem. Phys., 91 (1989) 1762

[S13] a) P.J. Hay and W.R. Wadt, J. Chem. Phys., 82 (1985) 270; b) W.R. Wadt and P.J. Hay, J. Chem. Phys., 82 (1985) 284; c) P.J. Hay and W.R. Wadt, J. Chem. Phys., 82 (1985) 299

[S14] a) P.J. Hay and W.R. Wadt, J. Chem. Phys., 82 (1985) 270; b) W.R. Wadt and P.J. Hay, J. Chem. Phys., 82

(1985) 284; c) P.J. Hay and W.R. Wadt, J. Chem. Phys., 82 (1985) 299; c) L.E. Roy, P.J. Hay, and R.L. Martin, J. Chem. Theory Comput., 4 (2008) 1029; d) A.W. Ehlers, M. Bohme, S. Dapprich, A. Gobbi, A. Hollwarth, V. Jonas, K.F. Kohler, R. Stegmann, A. Veldkamp, G. Frenking, Chem. Phys. Lett., 208 (1993) 111

[S15] O. M. Roscioni, E. P. F. Lee, and M. Dyke, J. Comp. Chem., 33 (2012) 2049

[S16] J. A. Pople, M. Head-Gordon, and K. Raghavachari, J. Chem. Phys., 87 (1987) 5968

[S17] Japan Chemical Society, Kagaku-Binran, Maruzen (1993) *in Japanese*

[S18] Gaussian 09, Rev. A. 02, M. J. Frisch, G. W. Trucks, H. B. Schlegel, G. E. Scuseria, M. A. Robb, J. R. Cheeseman, G. Scalmani, V. Barone, B. Mennucci, G. A. Petersson, H. Nakatsuji, M. Caricato, X. Li, H. P. Hratchian, A. F. Izmaylov, J. Bloino, G. Zheng, J. L. Sonnenberg, M. Hada, M. Ehara, K. Toyota, R. Fukuda, J. Hasegawa, M. Ishida, T. Nakajima, Y. Honda, O. Kitao, H. Nakai, T. Vreven, J. A. Montgomery, Jr., K. N. Kudin, V. N. Staroverov, R. Kobayashi, J. Normand, K. Raghavachari, A. Rendell, J. C. Burant, S. S. Iyengar, J. Tomasi, M. Cossi, N. Rega, J. M. Millam, M. Klene, J. E. Knox, J. B. Cross, V. Bakken, C. Adamo, J. Jaramillo, R. Gomperts, R. E. Stratmann, O. Yazyez, A. J. Austin, R. Cammi, C. Pomelli, J. W. Octerski, R. L. Martin, K. Morokuma, V. G. Zakrzewski, G. A. Voth, P. Salvador, J. J. Dannenberg, S. Dapprich, A. D. Daniels, O. Farkas, J. B. Foresman, J. V. Ortiz, J. Cioslowski, and D. J. Fox, Gaussian, Inc., Wallingford CT, 2009

[S19] R. Ditchfield, W. J. Hehre, and J. A. Pople, J. Chem. Phys., 54 (1971) 724

[S20] a) T. H. Dunning Jr., J. Chem. Phys., 90 (1989) 1007; b) R. A. Kendall, T. H. Dunning Jr., and R. J. Harrison, J. Chem. Phys., 96 (1992) 6796; c) A.K. Wilson, T. van Mourik, and T.H. Dunning Jr., J. Mol. Struct. (Theochem), 388 (1996) 339

[S21] S. Simon, M. Duran, and J. J. Dannenberg, J. Chem. Phys., 105 (1996) 11024-31.

[S22] a) G. Kresse, J. Hafner, Phys. Rev. B, 47 (1993) 558–561; b) G. Kresse, J. Hafner, Phys. Rev. B, 49 (1994) 14251–14269; c) G. Kresse, J. Furthmüller, Comput. Mater. Sci., 6 (1996) 15–50; d) G. Kresse, J. Furthmüller, Phys. Rev. B, 54 (1996) 11169–11186

[S23] a) P. E. Blöchl, *Phys. Rev. B*, 1994, **50**, 17953; b) G. Kresse, J. Joubert, Phys. Rev. B, 1999, 59, 1758

[S24] a) S. Grimme., J. Comp. Chem., 27 (2006) 1787; b) T. Bucko, J. Hafner, S. Lebègue, and J. G. Ángyán, J. Phys. Chem. A, 114 (2010) 11814-11824

[S25] S. Grimme, J. Antony, S. Ehrlich, and S. Krieg, J. Chem. Phys., 2010, 132, 154104

[S26] K. Momma, F. Izumi, J. Appl. Crystallogr., 44 (2011) 1272

[S27] Y. Maeda, K. Tada, and S. Yamazaki, e-J. Sur. Sci. Nanotech., 2018, **16**, 253-256